2015

Precise determination of the deuteron spin structure at low to moderate Q(2) with CLAS and extraction of the neutron contribution

N. Guler

S. E. Kuhn

Y. Prok

R. G. Fersch
College of William and Mary

P. Bosted
College of William and Mary

See next page for additional authors

Precise determination of the deuteron spin structure at low to moderate Q^2 with CLAS and extraction of the neutron contribution

N. Guler,[1,*] R. G. Fersch,[38,†] S. E. Kuhn,[1,‡] P. Bosted,[38,33] K. A. Griffioen,[38] C. Keith,[33] R. Minehart,[37] Y. Prok,[1,33] K. P. Adhikari,[1] D. Adikaram,[1,§] M. J. Amaryan,[1] M. D. Anderson,[36] S. Anefalos Pereira,[16] H. Avakian,[33] J. Ball,[8] M. Battaglieri,[17] V. Batourine,[33,23] I. Bedlinskiy,[21] A. Biselli,[10] W. J. Briscoe,[13] W. K. Brooks,[34,33] S. Bültmann,[1] V. D. Burkert,[33] D. S. Carman,[33] A. Celentano,[17] S. Chandavar,[26] G. Charles,[20] L. Colaneri,[18,29] P. L. Cole,[14,33] M. Contalbrigo,[15] D. Crabb,[37] V. Crede,[12] A. D'Angelo,[18,29] N. Dashyan,[39] A. Deur,[33] C. Djalali,[31] G. E. Dodge,[1] R. Dupre,[20] A. El Alaoui,[34] L. El Fassi,[1] L. Elouadrhiri,[33] P. Eugenio,[12] G. Fedotov,[31,30] S. Fegan,[17] A. Filippi,[19] J. A. Fleming,[35] T. A. Forest,[14] B. Garillon,[20] M. Garçon,[8] N. Gevorgyan,[39] G. P. Gilfoyle,[28] K. L. Giovanetti,[22] F. X. Girod,[33,8] J. T. Goetz,[26] E. Golovatch,[30] R. W. Gothe,[31] M. Guidal,[20] L. Guo,[11,33] K. Hafidi,[2] H. Hakobyan,[34,39] N. Harrison,[9] M. Hattawy,[20] K. Hicks,[26] D. Ho,[6] M. Holtrop,[24] S. M. Hughes,[35] C. E. Hyde,[1] D. G. Ireland,[36] B. S. Ishkhanov,[30] E. L. Isupov,[30] H. S. Jo,[20] K. Joo,[9] S. Joosten,[32] D. Keller,[37] M. Khandaker,[14,25] A. Kim,[9] W. Kim,[23] A. Klein,[1] F. J. Klein,[7] V. Kubarovsky,[33,27] S. V. Kuleshov,[34,21] K. Livingston,[36] H. Y. Lu,[31] M. Mayer,[1] I. J. D. MacGregor,[36] B. McKinnon,[36] M. Mirazita,[16] V. Mokeev,[33,30] R. A. Montgomery,[16] A Movsisyan,[15] C. Munoz Camacho,[20] P. Nadel-Turonski,[33,13] L. A. Net,[31] I. Niculescu,[22,13] M. Osipenko,[17] A. I. Ostrovidov,[12] K. Park,[33,23,‖] E. Pasyuk,[33] S. Pisano,[16] O. Pogorelko,[21] J. W. Price,[4] S. Procureur,[8] M. Ripani,[17] A. Rizzo,[18,29] G. Rosner,[36] P. Rossi,[33,16] P. Roy,[12] F. Sabatié,[8] C. Salgado,[25] D. Schott,[13] R. A. Schumacher,[6] E. Seder,[9] A. Simonyan,[39] Iu. Skorodumina,[31,30] D. Sokhan,[36] N. Sparveris,[32] I. I. Strakovsky,[13] S. Strauch,[31,13] V. Sytnik,[34] Ye Tian,[31] S. Tkachenko,[37] M. Ungaro,[33,9] E. Voutier,[20] N. K. Walford,[7] X. Wei,[33] L. B. Weinstein,[1] M. H. Wood,[5,31] N. Zachariou,[31] L. Zana,[35,24] J. Zhang,[33,1] Z. W. Zhao,[1,33] and I. Zonta[18,29]

(CLAS Collaboration)

[1]*Old Dominion University, Norfolk, Virginia 23529, USA*
[2]*Argonne National Laboratory, Argonne, Illinois 60439, USA*
[3]*Arizona State University, Tempe, Arizona 85287-1504, USA*
[4]*California State University, Dominguez Hills, Carson, California 90747, USA*
[5]*Canisius College, Buffalo, New York 14208, USA*
[6]*Carnegie Mellon University, Pittsburgh, Pennsylvania 15213, USA*
[7]*Catholic University of America, Washington, DC 20064, USA*
[8]*CEA, Centre de Saclay, Irfu/Service de Physique Nucléaire, 91191 Gif-sur-Yvette, France*
[9]*University of Connecticut, Storrs, Connecticut 06269, USA*
[10]*Fairfield University, Fairfield Connecticut 06824, USA*
[11]*Florida International University, Miami, Florida 33199, USA*
[12]*Florida State University, Tallahassee, Florida 32306, USA*
[13]*The George Washington University, Washington, DC 20052, USA*
[14]*Idaho State University, Pocatello, Idaho 83209, USA*
[15]*INFN, Sezione di Ferrara, 44100 Ferrara, Italy*
[16]*INFN, Laboratori Nazionali di Frascati, 00044 Frascati, Italy*
[17]*INFN, Sezione di Genova, 16146 Genova, Italy*
[18]*INFN, Sezione di Roma Tor Vergata, 00133 Rome, Italy*
[19]*INFN, Sezione di Torino, 10125 Torino, Italy*
[20]*Institut de Physique Nucléaire, CNRS/IN2P3 and Université Paris Sud, Orsay, France*
[21]*Institute of Theoretical and Experimental Physics, Moscow 117259, Russia*
[22]*James Madison University, Harrisonburg, Virginia 22807, USA*
[23]*Kyungpook National University, Daegu 702-701, Republic of Korea*
[24]*University of New Hampshire, Durham, New Hampshire 03824-3568, USA*
[25]*Norfolk State University, Norfolk, Virginia 23504, USA*
[26]*Ohio University, Athens, Ohio 45701, USA*
[27]*Rensselaer Polytechnic Institute, Troy, New York 12180-3590, USA*
[28]*University of Richmond, Richmond, Virginia 23173, USA*
[29]*Universita' di Roma Tor Vergata, 00133 Rome, Italy*
[30]*Skobeltsyn Institute of Nuclear Physics, Lomonosov Moscow State University, 119234 Moscow, Russia*
[31]*University of South Carolina, Columbia, South Carolina 29208, USA*
[32]*Temple University, Philadelphia, Pennsylvania 19122, USA*
[33]*Thomas Jefferson National Accelerator Facility, Newport News, Virginia 23606, USA*
[34]*Universidad Técnica Federico Santa María, Casilla 110-V Valparaíso, Chile*
[35]*Edinburgh University, Edinburgh EH9 3JZ, United Kingdom*
[36]*University of Glasgow, Glasgow G12 8QQ, United Kingdom*
[37]*University of Virginia, Charlottesville, Virginia 22901, USA*

[38]*College of William and Mary, Williamsburg, Virginia 23187-8795, USA*
[39]*Yerevan Physics Institute, 375036 Yerevan, Armenia*
(Received 2 June 2015; revised manuscript received 31 August 2015; published 2 November 2015)

We present the final results for the deuteron spin structure functions obtained from the full data set collected in 2000–2001 with Jefferson Lab's continuous electron beam accelerator facility (CEBAF) using the CEBAF large acceptance spectrometer (CLAS). Polarized electrons with energies of 1.6, 2.5, 4.2, and 5.8 GeV were scattered from deuteron ($^{15}ND_3$) targets, dynamically polarized along the beam direction, and detected with CLAS. From the measured double-spin asymmetry, the virtual photon absorption asymmetry A_1^d and the polarized structure function g_1^d were extracted over a wide kinematic range ($0.05\ \text{GeV}^2 < Q^2 < 5\ \text{GeV}^2$ and $0.9\ \text{GeV} < W < 3\ \text{GeV}$). We use an unfolding procedure and a parametrization of the corresponding proton results to extract from these data the polarized structure functions A_1^n and g_1^n of the (bound) neutron, which are so far unknown in the resonance region, $W < 2$ GeV. We compare our final results, including several moments of the deuteron and neutron spin structure functions, with various theoretical models and expectations, as well as parametrizations of the world data. The unprecedented precision and dense kinematic coverage of these data can aid in future extractions of polarized parton distributions, tests of perturbative QCD predictions for the quark polarization at large x, a better understanding of quark-hadron duality, and more precise values for higher-twist matrix elements in the framework of the operator product expansion.

DOI: 10.1103/PhysRevC.92.055201 PACS number(s): 13.60.Hb, 13.88.+e, 14.20.Dh

I. INTRODUCTION

One of the enduring goals in the field of hadron physics is a complete picture of how the fundamental particles of the standard model, quarks and gluons, make up the structure and the properties of the nucleon. Among other observables, the inclusive spin structure functions g_1 and g_2 of the nucleon are a vital ingredient for this picture (for a review, see Ref. [1]). For a complete understanding of the parton structure of the nucleon, we need precise and comprehensive data not only for the proton, but also for the neutron. Because the two nucleons are isospin partners, one can infer (assuming approximate isospin symmetry) the relative contribution from up and down valence quarks as a function of momentum fraction x from measurements on protons and neutrons. Furthermore, fundamental sum rules concerning the difference between proton and neutron structure functions at all values of squared four-momentum transfer Q^2 can be tested experimentally. The isoscalar sum of proton and neutron spin structure functions in the deep inelastic scattering (DIS) region is particularly sensitive, via perturbative QCD evolution equations [2–4], to the gluon helicity distribution inside a longitudinally polarized nucleon. Moments of structure functions from proton and neutron access different matrix elements of local operators within the operator product expansion (OPE) approach [5–7]. Finally, a better understanding of the phenomenon of quark-hadron duality [8,9] requires detailed studies of polarized as well as unpolarized structure functions of both nucleons in the resonance and DIS regions. While suitable free neutron targets do not exist, one can extract spin structure functions for a bound neutron using polarized nuclei like ^{2}H and ^{3}He, using some prescription to account for Fermi motion and the effective polarization of nucleons in nuclei. The results will be further affected to some extent by final state interaction (FSI) effects that are presently unknown. They have been estimated to be small in the DIS region [10] but may be larger in some part of the kinematic region covered by the data reported here. In the following, we quote results for the bound neutron without correcting for such FSI effects.

The CLAS collaboration at Jefferson Lab has collected a comprehensive set of spin structure function data on the proton as well as the deuteron over a wide range in $Q^2 \approx 0.05$–$5\ \text{GeV}^2$ and over a wide range of final state masses $W = 1$–3 GeV. A comparable data set has been collected for the neutron, using polarized ^{3}He as an effective neutron target and the spectrometers in Jefferson Lab's Hall A [11–13]. However, nuclear binding effects have to be accounted for in a model-dependent way to extract neutron structure functions from nuclear data. In particular, in the resonance region where cross sections and asymmetries may vary rapidly with W, Fermi smearing makes the extraction of neutron results challenging and somewhat ambiguous. For those reasons, neutron data extracted using an independent method and a different target, namely deuterium, are highly desirable, both to check systematic uncertainties and to more directly access the isoscalar combination $g_1^p + g_1^n$ and its moments. Some deuteron data in the resonance region exist from the RSS experiment [14], albeit over a relatively narrow range in Q^2. Many other experiments [15–19] have measured spin structure functions of the deuteron in the deep inelastic (DIS) region, $W > 2$ GeV and $Q^2 > 1\ \text{GeV}^2$, or at small x [20]. Very recently, the CLAS collaboration has published precise results from the EG1-dvcs run on the proton and the deuteron at the highest Q^2 accessible with Jefferson Lab so far [21].

With the experiment presented here (dubbed "EG1b") we collected a comprehensive data set on deuteron ($^{15}ND_3$, where D denotes the deuteron ^{2}H) targets with nearly equal statistical

*Current address: Spectral Sciences Inc., Burlington, MA 01803.
†Current address: Christopher Newport University, Newport News, VA 23606.
‡skuhn@odu.edu
§Current address: Thomas Jefferson National Accelerator Facility, Newport News, VA 23606.
‖Current address: Old Dominion University, Norfolk, VA 23529.

precision and kinematic coverage as on polarized protons ($^{15}NH_3$). The proton results will be published separately in the near future [22]. In this paper, we present our final results for the asymmetry $A_1(W,Q^2)$ and the spin structure function $g_1(x,Q^2)$ and its moments for the deuteron. The data were obtained in Jefferson Lab's Hall B during the time period 2000–2001. Previously, a much smaller data set on the deuteron was collected with CLAS in 1998 [23]. The present data set was taken with beam energies of 1.6, 2.5, 4.2, and 5.7 GeV. Preliminary results from the highest and lowest beam energies have been published [24–26]. The present paper includes, for the first time, the full data set collected with CLAS in 2000–2001 on the deuteron, including some of the experimental and analysis details particularly relevant for the deuteron ($^{15}ND_3$) target. We also provide, for the first time, our results for the corresponding (bound) neutron structure functions, based on a somewhat model-dependent deconvolution procedure which accounts for Fermi motion in the deuteron [27].

Our analysis of the deuteron data follows closely that for the proton data taken at the same time. Insofar as both analyses share the same ingredients and methods, only a brief summary is given here; the details will be provided in the future proton paper [22]. However, where the two analyses differ, we give all details specific to the deuteron in what follows. After a brief summary of formalism and theoretical background (Sec. II), we describe the experimental setup (Sec. III) and the analysis procedures (Sec. IV). We present the results for all measured and derived quantities, as well as models and comparison to theory, in Sec. V and offer our conclusions in Sec. VI.

II. THEORETICAL BACKGROUND

A. Formalism

We define the usual kinematic quantities in inclusive lepton scattering: incident (E) and scattered (E') lepton energy in the laboratory, scattering angle θ, energy transfer $\nu = E - E'$, and squared four-momentum transfer

$$Q^2 = -q^2 = \vec{q}^{\,2} - \nu^2 = 4EE'\sin^2\frac{\theta}{2}. \tag{1}$$

The invariant final-state mass is

$$W = \sqrt{M^2 + 2M\nu - Q^2}, \tag{2}$$

and the Bjorken scaling variable is

$$x = \frac{Q^2}{2M\nu}, \tag{3}$$

in which M is the nucleon mass. The variables

$$\gamma = \frac{2Mx}{\sqrt{Q^2}} = \frac{\sqrt{Q^2}}{\nu}, \quad \tau = \frac{\nu^2}{Q^2} = \frac{1}{\gamma^2}, \tag{4}$$

are also used, as well as the virtual photon polarization ratio

$$\epsilon = \left(1 + 2[1+\tau]\tan^2\frac{\theta}{2}\right)^{-1}. \tag{5}$$

B. Cross sections and asymmetries

The observable measured in EG1b is the double-spin asymmetry

$$A_{||}(\nu,Q^2,E) = \frac{d\sigma^{\uparrow\Downarrow} - d\sigma^{\uparrow\Uparrow}}{d\sigma^{\uparrow\Downarrow} + d\sigma^{\uparrow\Uparrow}} \tag{6}$$

for inclusive electron deuteron scattering with beam and target spin parallel ($\uparrow\Uparrow$) or antiparallel ($\uparrow\Downarrow$) along the beam direction. It depends on the four structure functions F_1^d, F_2^d, g_1^d, and g_2^d.[1] Introducing the ratio R of the longitudinal to transverse virtual photon absorption cross-sections,

$$R = \frac{\sigma_L}{\sigma_T} = \frac{F_2}{2xF_1}(1+\gamma^2) - 1, \tag{7}$$

and the variables

$$D = \frac{1 - E'\epsilon/E}{1+\epsilon R} \quad \text{and} \quad \eta = \frac{\epsilon\sqrt{Q^2}}{E - E'\epsilon}, \tag{8}$$

we can express $A_{||}$ as

$$\frac{A_{||}}{D} = (1+\eta\gamma)\frac{g_1}{F_1} + [\gamma(\eta-\gamma)]\frac{g_2}{F_1}. \tag{9}$$

Alternatively, the double-spin asymmetry $A_{||}$ can also be interpreted in terms of the two virtual photon asymmetries A_1 and A_2:

$$A_{||} = D[A_1(\nu,Q^2) + \eta A_2(\nu,Q^2)]. \tag{10}$$

Because of the relative size of the kinematic factors in Eqs. (9) and (10), our data are mostly sensitive to g_1 or A_1, which are the main quantities of interest (see Secs. II C and II D). Given a model or other information for F_1, R, and A_2, A_1 can be extracted directly from Eq. (10) and g_1 from

$$g_1 = \frac{\tau}{1+\tau}\left[\frac{A_{||}}{D} + (\gamma-\eta)A_2\right]F_1. \tag{11}$$

Our deuteron data are not sensitive enough to A_2 or g_2 to constrain these quantities; instead, a model based on other existing data is used (see Sec. V D).

C. Virtual photon absorption asymmetry

The asymmetry $A_1(W,Q^2)$ describes the relative strength for transverse (virtual) photon absorption on a nucleon leading to total final-state spin projection 1/2 vs 3/2 along the incoming photon direction. In the region of pronounced nucleon resonances (roughly at $W < 2$ GeV) it can be interpreted in terms of transition amplitudes to specific final states, $A_{3/2}$ (transverse photons leading to final state helicity 3/2) and $A_{1/2}$ (transverse photons leading to final state helicity 1/2),

[1] In principle, the tensor structure function b_1 also enters in the denominator, because any realistic polarized target will have a nonzero tensor polarization P_{zz}. However, in our case this is a subpercent correction because P_{zz} is expected to be less than 0.1 for our target [28] and the tensor asymmetry A_{zz} was measured by HERMES to be of order 0.01–0.02 [29].

with

$$A_1 = \frac{|A_{1/2}|^2 - |A_{3/2}|^2}{|A_{1/2}|^2 + |A_{3/2}|^2}. \quad (12)$$

In this case, the measured asymmetry A_1 at a given value of W gives information on the helicity structure of the combined resonant and nonresonant contributions to the inclusive cross-section, which can help to constrain the spin-isospin structure of nucleon resonances.

In the DIS region (at larger W and Q^2), $A_1(x)$ can yield information on the polarization of the valence quarks at sufficiently large x ($x \geqslant 0.5$), where they dominate. In the naive parton model, without taking nuclear effects into account, the limit of $A_{1d}(x)$ at large x is given as

$$A_{1d} \approx \frac{\Delta u_v + \Delta d_v}{u_v + d_v} = \frac{\Delta u_v/u_v + (d_v/u_v)\Delta d_v/d_v}{1 + d_v/u_v}, \quad (13)$$

where u_v,d_v are the unpolarized up and down valence quark distributions and Δu_v,Δd_v are the corresponding helicity distributions. In a SU(6)-symmetric, nonrelativistic quark model [30], $\Delta u/u = 2/3$ and $\Delta d/d = -1/3$, and $d/u = 1/2$, yielding $A_{1d} = 1/3$. However, more advanced quark models predict that $A_{1d}(x) \to 1$ as $x \to 1$ owing to SU(6) symmetry breaking [31]. However, even relativistic constituent quark models [32] predict a much slower rise towards $A_1 = 1$ than perturbative QCD calculations [33,34] incorporating helicity conservation. Recently, modifications of the pQCD picture to include orbital angular momentum [35] have yielded an intermediate approach towards $x = 1$. Precise measurements of A_1 at large x and in the DIS region are therefore required for protons, deuterons, and neutrons to establish the validity of these predictions.

D. The spin structure function g_1

The structure function $g_1(x, Q^2)$ contains important information on the internal spin structure of the nucleon. In the DIS limit (large Q^2 and ν), it encodes the polarized parton distribution functions (PDFs) $\Delta q(x) = q\uparrow(x) - q\downarrow(x)$ for quarks with helicity aligned vs antialigned with the overall (longitudinal) nucleon spin. Its logarithmic Q^2 dependence contains, via the QCD evolution equations [2–4], information on the analogous helicity-dependent gluon PDFs $\Delta G(x)$ as well. The deuteron, as an approximate isoscalar nucleon target, is particularly sensitive to $\Delta G(x)$, given a sufficiently large range in Q^2. Jefferson Lab data, like those presented in this paper, can serve as a valuable anchor point at the lowest possible Q^2 for next-to-leading-order (NLO) fits to extract $\Delta q(x)$ and $\Delta G(x)$.

In the region of lower Q^2, additional scaling violations occur due to higher-twist contributions, leading to correction terms proportional to powers of $1/Q^2$. These corrections can be extracted from our data because they cover seamlessly the transition from $Q^2 \ll 1$ GeV^2 to the scaling region $Q^2 > 1$ GeV^2. In the kinematic region where ν is also small and therefore $W < 2$ GeV, the structure of g_1 is dominated by the contributions from nucleon resonances (similarly to A_1).

However, as observed by Bloom and Gilman [8] for the unpolarized proton structure function F_2, there seems to be some duality between structure functions in the resonance region (averaged over a suitable range in W) and their extrapolated DIS values at the same quark momentum fraction x or $\xi = \frac{|\vec{q}|-\nu}{M}$. This correspondence should be tested for both nucleon species and for polarized as well as unpolarized structure functions to elucidate the underlying dynamics. EG1b data have uniquely suitable kinematic coverage stretching from the resonance to the DIS region to test whether duality holds for g_1. (An initial study of duality based on part of the EG1b data has been published [25].)

E. Quasielastic scattering

The virtual photon asymmetries A_1 and A_2 are also defined for elastic scattering off the nucleon and the same relationship Eq. (10) applies. One can show that $A_1 = 1$ in this case, and

$$A_2(Q^2) = \sqrt{R} = \frac{G_E(Q^2)}{\sqrt{\tau} G_M(Q^2)}, \quad (14)$$

where G_E and G_M are the electric and magnetic Sachs form factors of the nucleon.

One can also extend the definition of $g_1(x)$ and $g_2(x)$ for the nucleon to include elastic scattering, $x = 1$:

$$g_1^{\rm el}(x, Q^2) = \frac{1}{2}\frac{G_E G_M + \tau G_M^2}{1+\tau}\delta(x-1),$$
$$g_2^{\rm el}(x, Q^2) = \frac{\tau}{2}\frac{G_E G_M - G_M^2}{1+\tau}\delta(x-1). \quad (15)$$

For a bound system like deuterium, one has to consider the initial-state (Fermi) motion of the struck nucleons. In quasielastic inclusive scattering, $W \lesssim 1$ GeV, both the neutron and the proton contribute (weighed by their elastic cross sections). Alternatively, if one detects the struck proton in addition to the scattered electron with small missing four-momentum, the asymmetry $A_{||}$ will be close to that on a free proton [36]. In both cases, the theoretical asymmetry can be calculated with reasonable precision (given a realistic deuteron wave function) and therefore the measured asymmetry can be used to extract the product of target and beam polarization (see below).

F. Moments

In addition to the structure function $g_1(x)$ itself, its moments (integrals over x weighted by powers of x) are of great interest. Within the operator product expansion formalism, these moments can be related to local operators [5,6]. They are constrained by several sum rules and can be calculated directly within lattice QCD or in effective field theories like chiral perturbation theory (χPT) [37,38]. Determining these moments over a range of Q^2 allows us to study the transition from hadronic degrees of freedom at large distances (small Q^2) to partonic ones at small distances in our description of the nucleon and to extract higher-twist matrix elements that are sensitive to quark-gluon correlations in the nucleon.

The first moment of g_1,

$$\Gamma_1(Q^2) \equiv \int_0^1 g_1(x, Q^2) dx, \quad (16)$$

can be related to the contribution $\Delta\Sigma$ of the quark helicities to the nucleon spin in the limit of very high Q^2. In particular, for the average of proton and neutron (the isoscalar nucleon approximated by the deuteron) one has

$$\frac{\Gamma_1^{p+n}(Q^2\to\infty)}{2} \approx \Gamma_1^d = \frac{5}{36}(\Delta u + \Delta d) + \frac{1}{18}\Delta s. \quad (17)$$

Forming the difference between proton and the neutron yields the famous Bjorken sum rule [39,40],

$$\Gamma_1^p - \Gamma_1^n = \tfrac{1}{6}a_3 = 0.211, \quad (18)$$

where $a_3 = g_A = 1.267 \pm 0.004$ is the neutron axial β-decay constant.

At high but finite Q^2, these moments receive logarithmic pQCD corrections. At the more modest Q^2 of our data, additional corrections due to higher-twist matrix elements and proportional to powers of $1/Q^2$ become important:

$$\Gamma_1(Q^2) = \mu_2(Q^2) + \frac{M^2}{9Q^2}[a_2(Q^2) + 4d_2(Q^2) + 4f_2(Q^2)]\cdots. \quad (19)$$

Here μ_2 is the leading twist contribution given by Eq. (17) plus pQCD corrections, a_2 and d_2 are attributable to target mass corrections and f_2 is a twist-4 matrix element that contains information on quark-gluon correlations and has been calculated using quark models [41], QCD sum rules [42], and other approaches like lattice QCD [43].

In addition to the leading first moment, odd-numbered higher moments of g_1 can be defined as $\Gamma_1^n = \int_0^1 dx x^{n-1} g_1(x)$, $n = 3,5,7,\ldots$. These moments are dominated by high x (valence quarks) and are thus particularly well determined by data in Jefferson Lab kinematics. They can also be related to hadronic matrix elements of local operators or evaluated with lattice QCD methods. The third moment Γ_1^3 is related to the matrix element a_2 above.

In the limit of very small photon virtualities Q^2, moments of spin structure functions can be connected to observables in Compton scattering. In particular, the first moment is constrained by the Gerasimov-Drell-Hearn (GDH) sum rule [44,45] in the limit $Q^2 \to 0$,

$$\left.\frac{d\Gamma_1(Q^2)}{dQ^2}\right|_{Q^2=0} = -\frac{\kappa^2}{8M^2}, \quad (20)$$

where κ is the anomalous magnetic moment of the nucleon. Higher-order derivatives at the photon point are, in principle, calculable via χPT [37,38]. Therefore, measuring Γ_1 over the whole range in Q^2 yields a stringent test of our understanding of strongly interacting matter at all length scales.

Extending the analysis of low-energy Compton amplitudes to higher orders, one can get additional generalized sum rules [46]. In particular, one can generalize the forward spin polarizability, γ_0, to virtual photons:

$$\gamma_0(Q^2) = \frac{16\alpha M^2}{Q^6}\int_0^1 x^2\,[g_1(x,Q^2) - \gamma^2 g_2(x,Q^2)]\,dx. \quad (21)$$

Once again, this generalized spin polarizability can be calculated using χPT [38].

G. From nucleons to the deuteron

Most of the previous discussion is focused on the interpretation of spin structure functions of the nucleon (proton and neutron). Where appropriate, we indicate how this interpretation may be modified when the nucleons are embedded in deuterium. Here we want to discuss in more detail how the nuclear structure of the deuteron affects the measured asymmetries and structure functions.

In the most simple-minded picture, all observables on the deuteron can be considered (cross section weighted) averages of the corresponding proton and neutron observables. Spin observables are further modified by the fact that even in a fully polarized deuteron, the nucleon spins are not 100% aligned owing to the D-state component of the wave function. To first order, this can be corrected by applying a reduction factor $(1 P_D – 1.5 P_D)$ to all nucleon spin observables inside deuterium [47], with $P_D \approx 4\%–6\%$ being the D-state probability (according to the results from recent nucleon-nucleon potentials [48]). Taking this factor into account, the spin structure functions $g_1^d(x)$ and $g_2^d(x)$ of the deuteron are reasonably well approximated by the average of the proton and neutron ones, as long as x is not too large ($x < 0.6$) and W is not in the resonance region (i.e., $W > 2$ GeV). Moments of these structure functions can be considered as relatively "safe" because the integration averages over effects like Fermi motion [47].

In the valence region of moderate to large x and in the resonance region, Fermi-smearing due to the intrinsic motion of the nucleons inside deuterium as well as nuclear binding and FSI become more important, because structure functions vary rapidly in this region with W or x. These binding effects can be partially modeled by convoluting the free nucleon structure functions with the momentum distribution of nucleons inside deuterium. In our analysis, we use a recent convolution model by Melnitchouk *et al.* [27,49] that properly treats the effects of finite momentum transfer Q^2.

However, no universal model of the effects of FSI over the whole kinematic region covered by our data is available; we therefore do not correct for those effects. Similarly, potential off-shell effects (because of the negative binding energy of nucleons inside deuterium), including perhaps a modification of the nucleon structure (the EMC effect) and non-nucleonic degrees of freedom (mesons [50], $\Delta\Delta$ components [51,52], and perhaps more exotic quark structures [53]), may play a role. Because there is no universally accepted model for these effects, we present our results with the caveat that they are for bound neutrons only. Given the small binding energy (-2.2 MeV) and large average internucleon distance (of order 4 fm) in deuterium, we expect these effects to be significantly smaller than in more tightly bound nuclei. However, a comparison with neutron spin observables obtained from measurements on ^{3}He can be a valuable check on the size of nuclear binding corrections. Ultimately, the best approach to extracting free neutron information would be to apply the method of spectator tagging (pioneered for unpolarized structure functions in the recent "BONuS" experiment [54] at Jefferson Lab).

III. THE EXPERIMENT

The EG1b experiment took place at Jefferson Lab over a 7-month period in 2000–2001. It used the highly polarized (up to 85%) electron beam produced by the Continuous Electron Beam Accelerator Facility (CEBAF), with energies from 1.6 to nearly 6 GeV and currents of 0.3 to 10 nA in the experimental Hall B. Detailed descriptions of the accelerator and its strained GaAs polarized electron source can be found in Refs. [55–58].

The beam polarization was intermittently monitored using a Møller polarimeter, and the beam position and intensity distributions were measured with a set of beam monitors. The amount of beam charge delivered to the Hall for a given time interval was measured with a Faraday cup (FC). The signal from this FC was recorded separately for each beam polarization and gated by the data acquisition live time. To avoid local heating and depolarization, the beam was rastered over the face of the target in a spiral pattern, using two magnets upstream from the target.

The target consisted of cells containing samples of polarized hydrogen ($^{15}NH_3$), deuterium ($^{15}ND_3$), carbon, or no solid material ("empty target") that could be alternatively inserted in the beam. These cells were suspended in a liquid ^{4}He bath at about 1 K. The target material was polarized inside a 5-T solenoidal field along the beam axis, using the method of dynamic nuclear polarization (DNP) described in Refs. [59–61]. The target polarization was monitored by a nuclear magnetic resonance (NMR) system. Typical values of about 30% deuteron polarization along or opposite to the beam direction were achieved during the experiment.

Scattered electrons (and other particles) were detected with CLAS [62] in Hall B. CLAS employs a toroidal magnetic field and several layers of detectors in six identical sectors surrounding the beam axis for an acceptance of nearly 2π in azimuth. Electrons were detected in the scattering angle range from 8° to about 50°. Three regions of drift chambers (DC) [63] determine charged-particle trajectories, followed by Cherenkov counters (CC) [64] and electromagnetic calorimeters (EC) [65] for electron identification, while timing is provided by a scintillation counter (SC) system [66]. For EG1b, the trigger was optimized for inclusive electrons and required a coincidence between signals above threshold in the EC and the CC.

The experimental setup and operation will be described in detail in the upcoming companion paper on our proton results [22].

IV. DATA ANALYSIS

A. Data set

Data on the deuteron (ND_3) were taken with seven different beam energies and two opposite polarities of the CLAS torus magnetic field. For positive (+) polarity, electrons are bent towards the beamline, and for the negative (−) polarity, they are bent away from it. The inbending (+) configuration gives access to the largest scattering angles and allows CLAS to run with its highest possible luminosity of $L = 2 \times 10^{34}\,\mathrm{cm}^{-2}\,\mathrm{s}^{-1}$. Therefore, we used this configuration to collect the highest Q^2 points for each beam energy. In the outbending (−) configuration, electrons were detected down to the smallest accessible scattering angle of 8°, extending the data set to lower Q^2.

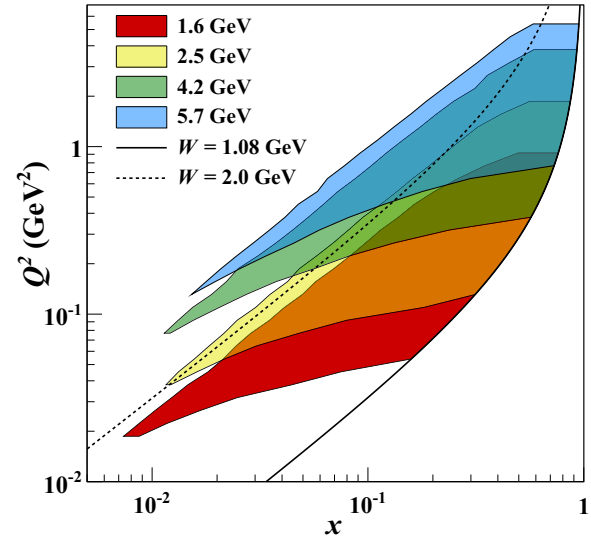

FIG. 1. (Color online) Kinematic coverage in Q^2 vs x for each of the four main electron beam energy groupings used in the EG1b experiment. The solid and dotted lines denote the $W = 1.08$-GeV and $W = 2.00$-GeV thresholds, respectively. The coverages for proton (NH_3) and deuterium (ND_3) targets were nearly identical.

In all, data were collected in 11 specific combinations (1.606+, 1.606−, 1.723−, 2.561+, 2.561−, 4.238+, 4.238−, 5.615+, 5.725+, 5.725−, 5.743−) of beam energy (in GeV) and main torus polarity (+,−), hereby referred to as "sets." Sets with similar beam energy comprise four groupings with nominal average energies of 1.6, 2.5, 4.2, and 5.7 GeV. The kinematic coverage of the data for each of the four energy groupings is depicted in Fig. 1.

B. Data selection

After following the standard calibration procedures for all CLAS detector elements, the raw data were converted into a condensed data summary tape (DST) format containing track and particle ID information. Quality checks ensured that malfunctioning detector components, changes in the target, and/or potential sources of false asymmetries did not contaminate the data. DST files not meeting the minimal requirements were eliminated from analysis.

Event selection criteria were applied to identify scattered electrons and to minimize the background from other particles, primarily π^-. These criteria, based on the signals from the CC and the EC, will be discussed in detail in Ref. [22]. We ascertained that the remaining π^- contamination of our electron sample was less than 1% over the whole kinematic range. For this reason, we assign a 1% systematic uncertainty on our extracted asymmetries as an upper limit for any remaining pion contamination effect.

For the determination of the product of beam and target polarization ($P_b P_t$; see below) as well as kinematic corrections, we also required a sample of quasielastic $(e,e'p)$ events.

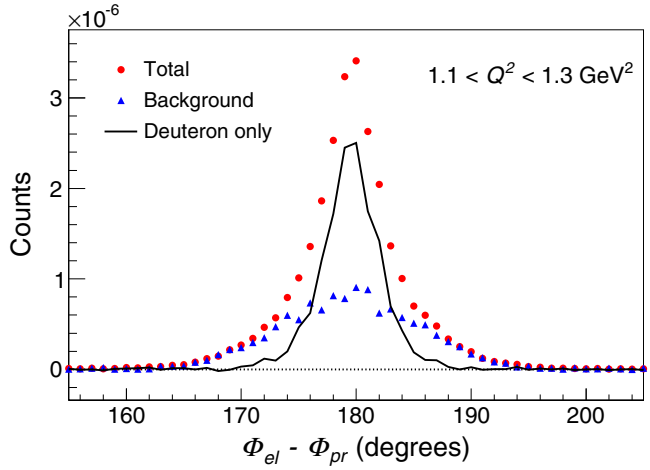

FIG. 2. (Color online) Distribution of quasielastic $d(e,e'p)$ events versus the angle ϕ between the azimuth of the scattered electron and the azimuth of the observed proton. The background due to nitrogen, liquid ^{4}He, and various foils is strongly suppressed by the cuts described in the text, leading to a relatively clean signal from the deuteron component (solid line) of the target. A final cut is applied from $\phi = 177^\circ$ to $\phi = 183^\circ$.

We selected ep coincidences through a timing cut of ± 0.8 ns on the difference between the reconstructed electron and proton vertex time. Quasielastic events were selected through cuts on W, $0.89\ \text{GeV} \leqslant W \leqslant 1.01\ \text{GeV}$, missing energy (of the unobserved nuclear remnant) of $\leqslant 0.08$ GeV (kinetic), and on the difference between the polar ($|\Delta\theta| \leqslant 2^\circ$) and azimuthal ($|\Delta\phi| \leqslant 3^\circ$) angles of the detected proton and the reconstructed direction of the virtual photon. These cuts were optimized to include most of the ep coincidences from quasielastic scattering on the deuteron, while the contribution from the other target components (nitrogen, ^{4}He, and foils) was much suppressed owing to the wider nucleon momentum distributions in these nuclei (see Fig. 2).

C. Event corrections

The track information for particles in the DSTs is based on an ideal detector and has to be corrected for various effects from detector materials and imperfections. Among other corrections, energy loss due to ionization in the target (both for the incoming and the scattered electron), multiple scattering angle deviations (compared to the average vertex of all particles in an event), and known deviations of the target magnetic field from the ideal version implemented in the reconstruction software were used to correct each track within an event.

The reconstruction software also assumes that a track originates on the nominal central axis ($x = y = 0$) of CLAS. In reality, the beam is rastered over a circle of about 1.5 cm diameter, whose center is typically offset by a few mm from the nominal axis. Since the raster position can be inferred from the currents in the raster magnets, the reconstructed vertex was corrected for this offset.

The position and orientation of the DC in space and the detailed three-dimensional shape of the torus magnetic field are not known with absolute precision; an empirical parametrization of their deviations from the ideal detector was obtained from a fit to data from the companion experiment on the proton [22]. We used four-momentum conservation in fully exclusive events like $\text{H}(e,e'p)$ and $\text{H}(e,e'p\pi^+\pi^-)$ to optimize the fit parameters. This parametrized correction for particle momenta and scattering angles was then applied to each track. The resulting improvement of the resolution in the missing mass W is shown in Fig. 3.

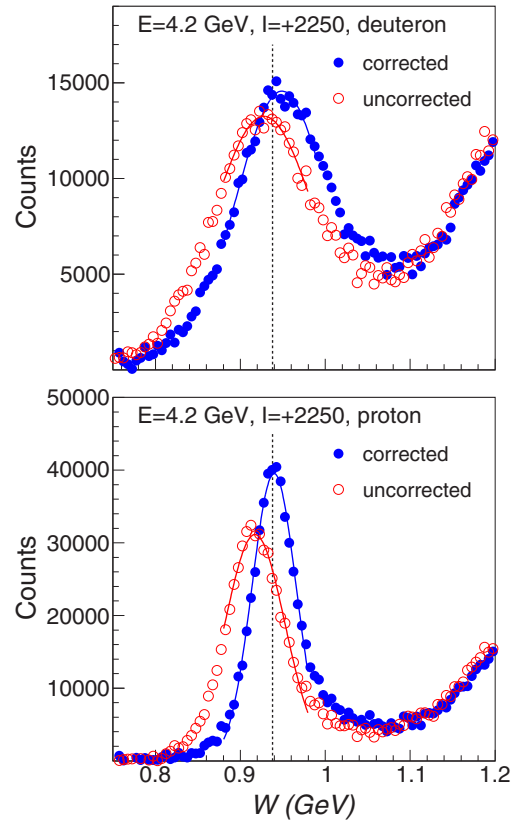

FIG. 3. (Color online) Missing mass W before (red open circles) and after (blue solid circles) the kinematic corrections for the 4.238+ data set for NH_3 (top) and ND_3 (bottom) targets. The corrections decreased the distribution width and centered the mean value of the (quasi-)elastic peak on the nucleon mass.

A final correction was applied to the integrated beam charge measured by the Faraday cup (FC) to account for beam loss between the target and the FC due to multiple scattering and dispersion by the target magnetic field.

D. From raw to physics asymmetries

For each combination of beam energy, torus polarity, and target polarization, electron tracks were sorted by kinematic bins and were counted separately for positive (N^+) and negative (N^-) beam helicity, where "+" refers to a beam helicity antiparallel to the direction of the target polarization. These counts were normalized to the corresponding integrated Faraday charges, $n^\pm = N^\pm / FC^\pm$. Only events coming from complete pairs of "beam buckets" with opposite helicity were counted to avoid false asymmetries; we also ascertained that,

after averaging over all target polarizations, the residual beam charge asymmetry $(FC^+ - FC^-)/(FC^+ + FC^-)$ was less than 10^{-4}. These normalized counts were used to form the raw asymmetry

$$A_{\rm raw} = \frac{n^+ - n^-}{n^+ + n^-} \tag{22}$$

in each kinematic bin. This raw asymmetry was then converted to the desired physics asymmetry $A_{||}$ [Eq. (6)] by applying a series of corrections which we now discuss in sequence.

1. Dilution factor

The dilution factor $F_{\rm DF} \equiv n_d/n_A$ is defined as the ratio of events from polarizable nuclei of interest (here deuterons bound in ammonia, n_d) to those from all components of the full ammonia target (n_A). It is calculated directly from the radiated cross-sections on all components of the target. In terms of densities (ρ), material thicknesses (ℓ), and cross-sections per nucleon (σ),

$$n_d \propto \tfrac{6}{21}\rho_A \ell_A \sigma_d \tag{23}$$

and

$$n_A \propto \rho_{Al}\ell_{Al}\sigma_{Al} + \rho_K \ell_K \sigma_K + \rho_A \ell_A \left(\tfrac{6}{21}\sigma_d + \tfrac{15}{21}\sigma_N\right) + \rho_{He}(L - \ell_A)\sigma_{He}, \tag{24}$$

with the subscripts A, Al, K, N, and He denoting deuterated ammonia ($^{15}ND_3$), aluminum foil, kapton foil, nitrogen (^{15}N), and helium (^{4}He), respectively. The acceptance-dependent proportionality constant is identical in both of the above relations for a given kinematic bin. Inclusive scattering data from the empty, i.e. liquid Helium (LHe), and ^{12}C targets were analyzed to determine the total target cell length (L) and effective ND_3 thickness (ℓ_A) using similar equations.

The required cross sections were calculated from a fit to world data for F_1 and F_2 for protons and neutrons, using a Fermi-convolution model to fit inclusive scattering data on nuclear targets, including EG1b data from ^{12}C, solid ^{15}N and empty (LHe) targets [67,68]. The nuclear EMC effect was parametrized using Stanford Linear Accelerator Center (SLAC) data [69]. Radiative corrections used the treatment of Mo and Tsai [70]; external bremsstrahlung probabilities incorporated all material thicknesses in CLAS from the target vertex through the inner layer of the DC.

Dilution factors $F_{\rm DF}$ were calculated for each data set and used to correct the raw asymmetry,

$$A_{\rm undil} = \frac{A_{\rm raw}}{F_{\rm DF}}, \tag{25}$$

to get the undiluted asymmetry due to deuterons in the target. We checked our results for $F_{\rm DF}$ from the "standard method" described above against a previously developed "data-based method" [24,26,71] that uses a simple model of neutron-proton cross-section ratios to express the background in the ammonia target in terms of the counts from carbon and empty targets. Values of L and ℓ_A varied by less than 2% between the two methods. Figure 4 shows the result from both methods for four kinematic bins. For the inelastic data, $W > 1.1$ GeV, the dilution factors from the cross-section-based standard method were more precise and were used to correct the raw asymmetries. We used the data-based method only in the quasielastic region $W < 1.08$ GeV (for the determination of beam and target polarization in one case, see below) and to subtract the background from exclusive $d(e,e'p)n$ events (see Fig. 2). This is because finite detector resolution effects (which are not included in the cross-section model) significantly affect the shape of sharply peaked spectra in the quasielastic region, making the data-driven method more reliable.

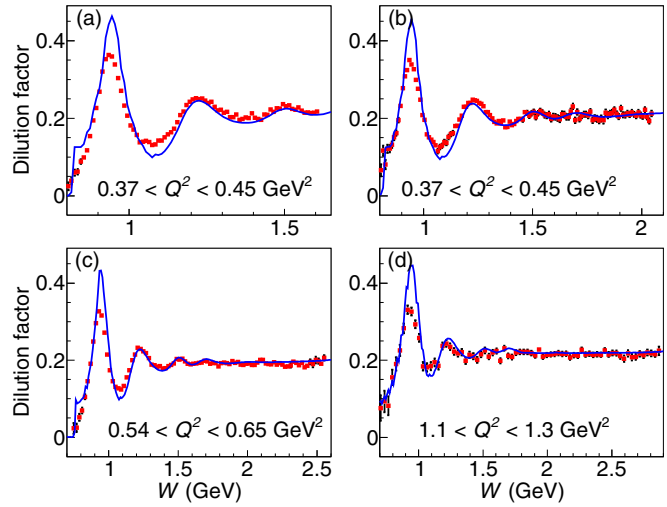

FIG. 4. (Color online) Dilution factors as a function of W, shown for four different combinations of beam energies and torus polarity [1.6+ (a), 2.5− (b), 4.2− (c), and 5.7− (d)]. The results from our standard method (using cross-section models; see text) are shown as blue lines, while the results from the data-based method (see text) are shown as the red data points.

The densities and thicknesses of all target materials were varied within their known tolerances to determine systematic uncertainties; only the variations of $\rho_C \ell_C$ and ρ_{He} had any significant (<1%) effect on $F_{\rm DF}$. Uncertainties due to the cross-section model were estimated by the comparison of $F_{\rm DF}$ to a third-degree polynomial fit to the data-based dilution factors determined by the alternate method.

2. Beam and target polarizations ($P_b P_t$)

The second major factor to consider when extracting the physics asymmetry $A_{||}$ is the product of beam and target polarization by which the measured asymmetry must be divided.

Because NMR measurements provided accurate target polarization measurements only near the edge of the target cell [72] (which was not uniformly exposed to the beam), we determined the polarization product $P_b P_t$ directly from our data, using quasielastic $d(e,e'p)n$ and (in one case) $d(e,e')$ events. Here we made use of the fact that the theoretical asymmetry in this case depends only on the electromagnetic form factors of the proton and the neutron (see Sec. II E), which are well-known [73], giving us reliable predictions of $A_{||}$. After correcting for the (relatively smaller) dilution of this asymmetry from nondeuterium components of the target, we can directly divide the measured $A_{||}$ by the theoretical one to

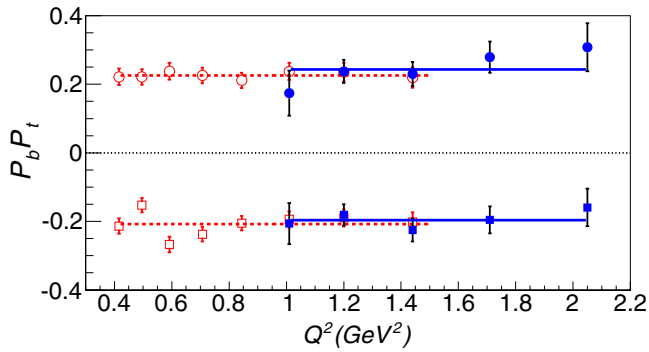

FIG. 5. (Color online) $P_b P_t$ values for the 2.5-GeV inbending data sets. The plot shows the resulting $P_b P_t$ values extracted independently for each Q^2 bin with available data. The results from the exclusive (blue solid symbols) and the inclusive (red open symbols) methods are shown. The corresponding constants fit to the data are also shown as lines: The solid blue line is for the exclusive and the dashed red line is for the inclusive method.

extract $P_b P_t$:

$$P_b P_t = \frac{A_{\rm meas}^{\rm QE}}{F_{\rm DF}\, A_{\rm theo}^{\rm QE}}. \tag{26}$$

We used the value for $P_b P_t$ obtained from inclusive quasielastic $d(e,e')$ events only in one case, for the 1.6–1.7 GeV outbending configuration runs. In that case, too few of the protons from $d(e,e'p)n$ were detected in CLAS for a reliable determination of $P_b P_t$. We used a cut of $0.89\ {\rm GeV} \leqslant W \leqslant 1.01\ {\rm GeV}$ to define quasielastic events. While this method yields a smaller statistical uncertainty, it has greater systematic uncertainty because of larger background contributions; therefore, a systematic uncertainty of 10% was assigned to this particular $P_b P_t$ value. This uncertainty was obtained by varying the relative normalization of the carbon and empty target data used to estimate the background within reasonable limits, consistent with the observed tails of the W spectra from all three targets.

For all other configurations, we determined $P_b P_t$ using exclusive $d(e,e'p)n$ events within the cuts listed in Sec. IV B which have very little background from nuclear target components (see Fig. 2). We used a detailed Monte Carlo simulation, including Fermi motion of the proton inside the deuteron, to calculate the theoretical asymmetry. For both methods, the nuclear background was determined using the data-driven method mentioned in Sec. IV D 1. As a cross-check, we compared these results to the values derived from inclusive quasielastic scattering and found them generally to be consistent within the statistical uncertainty.

The derived $P_b P_t$ values were checked for consistency across Q^2 for each beam energy, torus current, and target polarization direction. Sample $P_b P_t$ values across Q^2 for two beam energies are shown in Fig. 5. Across all beam energies, $P_b P_t$ values ranged from 0.1 to 0.28, with most values between 0.15 and 0.25. We varied each of the values of $P_b P_t$ individually by the larger of one (statistical) standard deviation and the difference between the exclusive and inclusive results to assess the systematic uncertainty of all physics quantities due to $P_b P_t$.

3. Polarized nitrogen and target contamination corrections

Apart from the dilution of the measured asymmetry by nucleons embedded in nitrogen, helium, and other target materials (Sec. IV D 1), there are additional small modifications of this asymmetry owing to polarized target nucleons outside of deuterium.

First, it is well-known that the ^{15}N nuclei in the ammonia molecules become somewhat polarized as well. Equal spin temperature (EST) theory predicts the polarization ratio between two spin-interacting nuclear species in a homogenous medium as the ratio of their magnetic moments: $P_{^{15}{\rm N}}/P_{^2{\rm H}} \approx \mu_{^{15}{\rm N}}/\mu_{^2{\rm H}}$. However, experimentally, it was found that the ^{15}N polarization is somewhat smaller than that [74]. Using a simple shell-model description [75] of the ^{15}N nucleus, this polarization is carried by a single proton in the $1p_{1/2}$ shell, which means that this proton is spin polarized to -33% of the nucleus. The measured magnetic moment of ^{15}N suggests a somewhat smaller spin polarization, so that the overall contribution from nitrogen to the measured asymmetry can be approximated by that of a bound proton with polarization $P_p^{\rm bound}$ between 8% and 16% of the deuteron polarization. Accordingly, we subtracted a correction of $1/3 \times P_p^{\rm bound} \times A_p \sigma_p^{\rm bound}/\sigma_d \approx (0.026 \pm 0.014) A_p$ from the measured asymmetry, where the factor $1/3$ accounts for the three deuteron nuclei per nitrogen nucleus in ammonia.

A second contamination to the measured asymmetry comes from isotopic impurities of the deuterated ammonia, with some deuterons replaced with protons. Typical contaminations quoted in the literature [15] are around 1.5%. We did a careful study [76] that showed a ^{1}H contamination of up to about 3.5% during EG1 (which was included in the dilution factor); however, according to this study at most one-half of these extra protons were polarized (the remainder are presumably bound in molecules like H_2O and are unpolarized). The degree of polarization of these protons can be estimated as $P_p/P_d \approx 1.2$–1.5, again according to EST and empirical evidence [75]. The net effect is an additional term proportional to A_p that has to be subtracted from the measured asymmetry. The total correction for bound and free polarized protons in the target is between $0.027 A_p$ and $0.051 A_p$. We took the median of this range to correct our data (using a model of the asymmetry A_p based on our proton results [22]) and $1/2$ of its spread to estimate systematic uncertainties. An additional correction owing to the very small contribution of ^{14}N nuclei (less than 2% of our ammonia sample) was too small to be applied but was included in the overall systematic uncertainty.

Quasielastic $d(e,e'p)n$ events are also affected by the various target contaminations discussed above. We applied a corresponding correction to our extraction of $P_b P_t$ (Sec. IV D 2).

4. Other background subtractions

Dalitz decay of neutral pions [77] and Bethe-Heitler processes [78] can produce e^+e^- pairs at or near the vertex, contaminating the inclusive e^- spectrum. This contamination was at most a few percent of the data rate (at high W)

and was measured by comparing positron and electron rates for runs with opposite torus polarity. We also measured the positron asymmetry and found it consistent with zero. We subtracted this pair-symmetric background using the measured rate and assuming zero asymmetry. To estimate the corresponding systematic uncertainty, we instead applied a correction assuming a constant positron asymmetry within the range of values we measured. We also used the change in the correction after varying the rate within its uncertainty as a second contribution to the overall systematic uncertainty for this background.

5. *Radiative corrections*

Radiative corrections to the measured asymmetries $A_{||}$ were computed using the program RCSLACPOL, which was developed at SLAC for the spin structure function experiment E143 [69]. Polarization-dependent internal and external corrections were calculated according to the prescriptions in Ref. [79] and Ref. [70], respectively.

We compared the calculated double-spin asymmetry with radiative effects turned on, A_r, to the Born asymmetry, A_B, calculated with the same models (see Sec. V D). We determined parameters $f_{\rm RC}$ and $A_{\rm RC}$ for each kinematic bin, allowing us to write the Born asymmetry as

$$A_B = \frac{A_r}{f_{\rm RC}} + A_{\rm RC}, \tag{27}$$

where $f_{\rm RC}$ is a radiative dilution factor accounting for the count rate fraction from the elastic and quasielastic tail within a given bin. This correction was then applied to all data. Figure 6 shows a few examples for the magnitude of the correction, together with the final data for the Born asymmetry $A_{||}$.

Systematic uncertainties on these corrections were estimated by running RCSLACPOL for a range of reasonable variations of the models for F_2, R, A_1, and A_2 (see Sec. V D) and for different target thicknesses and cell lengths, ℓ_A and L. The changes due to each variation were added in quadrature and the square root of the sum was taken as the systematic uncertainty on radiative effects.

6. *Systematic uncertainties*

Estimation of systematic uncertainties on each of the observables discussed in the following section was done by varying a particular input parameter, model, or analysis method, rerunning the analysis, and recording the difference in output for each of the final asymmetries, structure functions, and their moments. Final systematic uncertainties attributable to each altered quantity were then added in quadrature to estimate the total uncertainty. Note that for each quantity of interest (A_1, g_1, Γ_1) the systematic uncertainty was calculated by this same method (instead of propagating it from other quantities), therefore ensuring that all correlations in these sources were properly taken into account.

Most sources of systematic uncertainties have been discussed above. These sources include kinematic shifts, bin averaging, target parameters (radiative corrections), nuclear dilution model, structure function models, $P_b P_t$ uncertainty for each individual data set, and background contaminations.

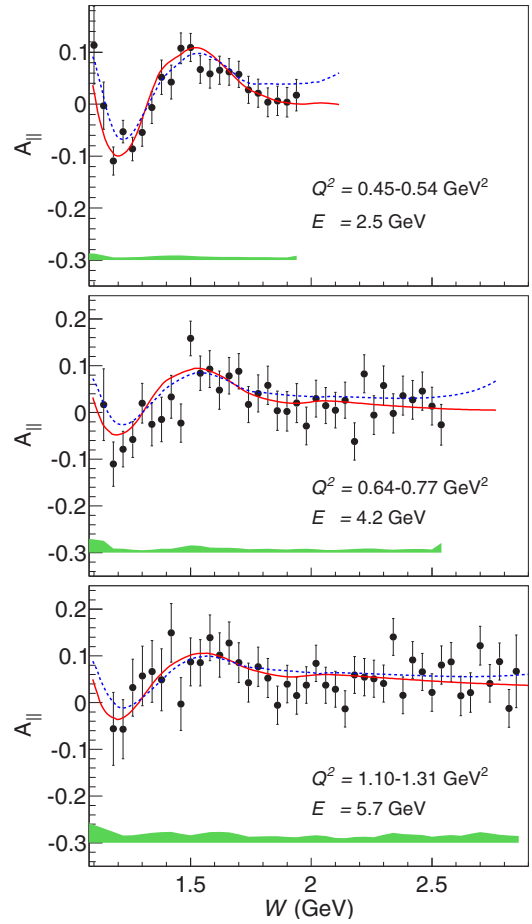

FIG. 6. (Color online) Representative results for the fully corrected double-spin asymmetry $A_{||}$ versus final state invariant mass W for three different Q^2 bins and beam energies. The red solid line represents our model parametrization of $A_{||}$ (see Sec. V D). The dashed blue lines represent the model including radiative effects. The difference between those lines corresponds to the magnitude of radiative corrections applied. The error bars reflect statistical uncertainties while the shaded bands at the bottom of each plot represent the total systematic uncertainties.

The relative magnitudes of these various contributions to the systematic uncertainty, for the case of the ratio g_1/F_1, are listed in Table I. The results shown in the next section incorporate these systematic uncertainties.

TABLE I. Table of typical magnitudes for various systematic uncertainties.

Systematic uncertainty	Typical range (in % of g_1/F_1)
Pion and e^+e^- contamination	0.0–1.0
Dilution factor	1.8–2.7
Radiative corrections	3.5–5.7
$P_b P_t$ uncertainty	6–22
Model uncertainties	2.0–5.0
Polarized background	1.0–1.7
Total	10–23

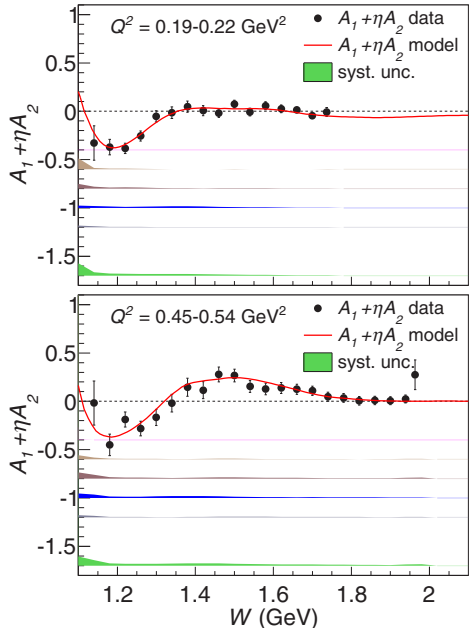

FIG. 7. (Color online) Representative values for the double-spin asymmetry $A_1 + \eta A_2$ versus final-state invariant mass W. The top panel is for 0.16 GeV$^2 \leqslant Q^2 \leqslant$ 0.19 GeV^2 (1.6-GeV data) and the bottom panel for 0.45 GeV$^2 \leqslant Q^2 \leqslant$ 0.54 GeV^2 (2.5-GeV data). The red solid line represents our model parametrization of $A_1 + \eta A_2$ (see Sec. V D). The shaded band at the bottom (green) is the total systematic uncertainty. The individual contributions are offset vertically, from top to bottom: pion and pair symmetric contamination (-0.4; barely visible); dilution factor (-0.6); $P_b P_t$ (-0.8); models plus radiative corrections (-1.0); and polarized background (-1.2).

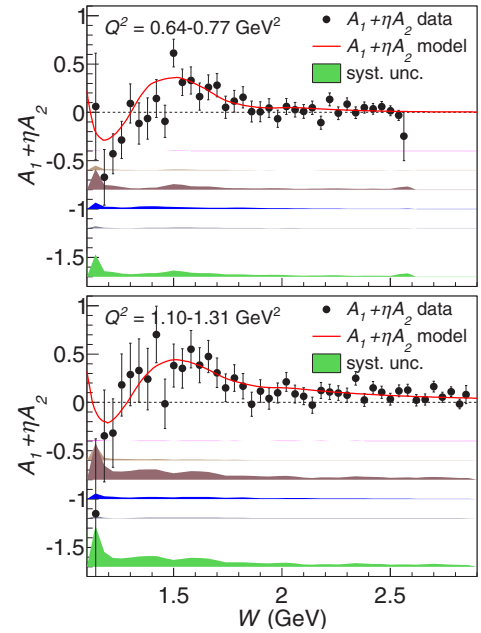

FIG. 8. (Color online) Same as Fig. 7, except for two higher beam energies. The top panel is for 0.64 GeV$^2 \leqslant Q^2 \leqslant$ 0.77 GeV^2 (4.2-GeV data) and the bottom panel for 1.1 GeV$^2 \leqslant Q^2 \leqslant$ 1.3 GeV^2 (5.7-GeV data).

V. RESULTS AND COMPARISON TO THEORY

A. Results for $A_1 + \eta A_2$

In this section, we present our final results for all quantities of interest: A_1, g_1, and moments for the deuteron and the bound neutron. As a first step, we divide the fully corrected Born asymmetry $A_{||}$ by the depolarization factor D [Eq. (8)] to extract the combination $A_1 + \eta A_2$ for each bin in W and Q^2 and each beam energy. Results for similar beam energies (e.g., 1.6 and 1.7 GeV) and inbending and outbending torus polarization are combined into averaged values for four nominal energies (1.6, 2.5, 4.2, and 5.7 GeV), weighted by their statistical precision. We checked that in each case, the data sets that we combined agree with each other within statistical and systematic uncertainties. Figures 7 and 8 show the results for $A_1 + \eta A_2$ for selected Q^2 bins and for each of the four standard energies. The systematic uncertainties from different contributing sources are also shown as shaded bands at the bottom of each plot. For most kinematics, the largest contribution to the systematic uncertainty is attributed to the beam and target polarization, with some contribution from the dilution factor and radiative corrections. We note that our data for all four beam energies are well described by our model (see Sec. V D), as indicated by the red solid line.

Our results for $A_1 + \eta A_2$ have the least theoretical bias from unmeasured structure functions like A_2 and F_1 and are therefore the preferred choice for NLO fits that will include our data in the high-Q^2, high-W region, like the fit by the JAM collaboration [80]. They can be found in the CLAS database [81] and in the Supplemental Material [82] for this paper.

B. The virtual photon asymmetry A_1

Once $A_1 + \eta A_2$ is calculated, we can extract the virtual photon asymmetry A_1, by using a model for A_2 (see Sec. V D). Because A_1 depends only on W and Q^2, we can combine the results from all beam energies at this stage, again weighted by statistical uncertainties. Figure 9 shows $A_1(W)$ for three representative Q^2 bins together with different sources of systematic uncertainties. The uncertainty on A_2 (included in the band at -1.0) is the dominant contribution to the overall systematic uncertainty (shaded band at the bottom of each panel).

Figures 10 and 11 show A_1 versus W for all Q^2 bins in our kinematic coverage, as well as existing data from SLAC E143 [15,83] and from the Jefferson Lab RSS experiment [14,84]. Gaps are attributed to a lack of kinematic coverage between the different beam energies. Data points with very large statistical or systematic uncertainties were omitted from these plots.

At all but the highest Q^2, the effect of the $\Delta(1232)3/2^+$ resonance is clearly visible in the strongly negative values of A_1, owing to the dominance of the $A_{3/2}$ transition to this resonance. At our lowest Q^2, the asymmetry is, in general, negative or close to zero, which proves that the $A_{3/2}$ transition amplitude is dominant in this region, as expected from exclusive pion production. As we go to higher values of Q^2 and W, the transition amplitude $A_{1/2}$ leading to resonances such as $N(1520)3/2^-$ and $N(1535)1/2^-$ becomes dominant,

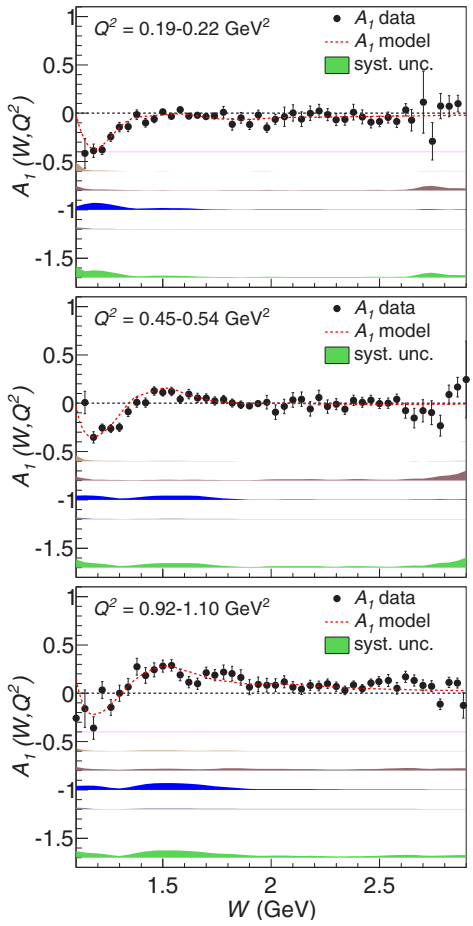

FIG. 9. (Color online) Virtual photon asymmetry A_1 for the deuteron versus W for a few Q^2 bins: 0.16 GeV$^2 \leqslant Q^2 \leqslant$ 0.19 GeV^2 (top), 0.45 GeV$^2 \leqslant Q^2 \leqslant$ 0.54 GeV^2 (middle), and 1.1 GeV$^2 \leqslant Q^2 \leqslant$ 1.3 GeV^2 (bottom). The statistical uncertainties are indicated by error bars, while the total systematic uncertainties are indicated by the shaded band at the bottom. Again, the individual contributions are shown separately as offset bands: pion and pair symmetric contamination (−0.4); dilution factor (−0.6); $P_b P_t$ (−0.8); models plus radiative corrections (−1.0); and polarized background (−1.2).

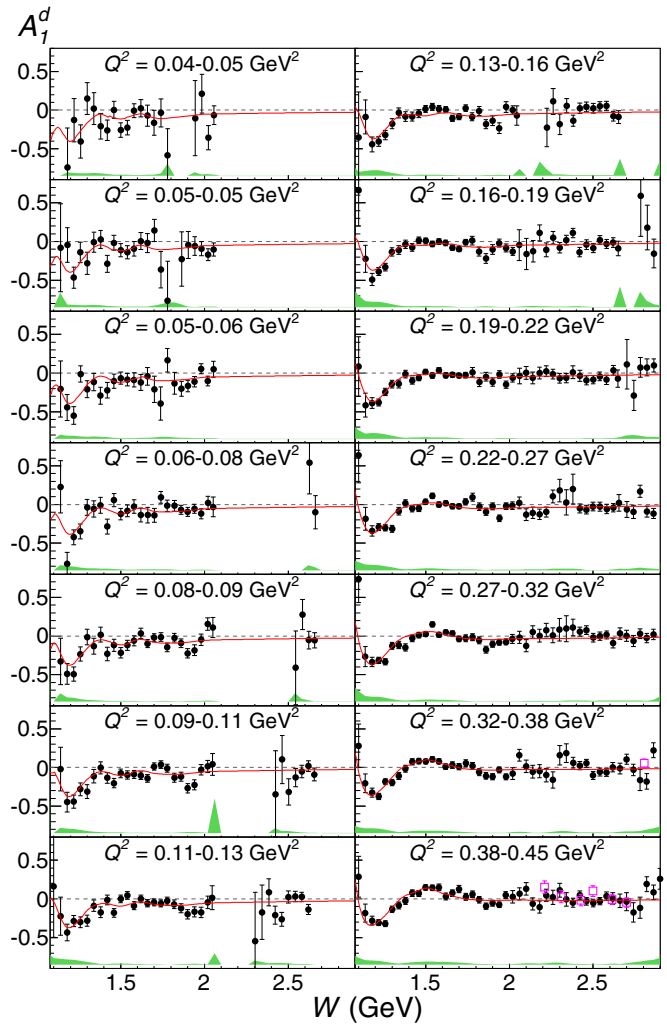

FIG. 10. (Color online) A_1 for the deuteron versus W for our 14 lowest Q^2 bins. Total systematic uncertainties are shown as a shaded area at the bottom of each plot. Our parametrized model is also shown as a red line on each plot. Only the data points with $\sigma_{\text{stat}} < 0.3$ and $\sigma_{\text{sys}} < 0.2$ are plotted. In addition, we also show data from SLAC E143 [15,83] (open magenta squares).

as expected from pQCD. At $W > 2$ GeV and larger Q^2, the asymmetry continues smoothly from the resonance region into the DIS region where it has been measured by previous experiments to be positive, because of the larger contribution from the proton (with $A_1 > 0$ throughout the measured x range in the DIS region).

This trend becomes more apparent if we integrate our data on A_1 over the full measured DIS range with $W > 2$ GeV and $Q^2 > 1$ GeV^2 and plot it as a function of the scaling variable x. The behavior of $A_1(x)$ at large x is of high interest to test various models inspired by QCD, as outlined in Sec. II C. Figure 12 shows this quantity from EG1b together with world data and various models. We note that our data lie somewhat below most of the world data, which is partially explained by the fact that at each point in x, they have the lowest average Q^2 of all the experiments shown, implying a more significant impact of scaling violations due to higher-twist effects. In particular, the new results from EG1-dvcs [21] (also shown in Fig. 12) are for 5.9-GeV beam energy and scattering angles above 18°, while our data average over 5.7 and 4.2 GeV and scattering angles down to 8°. In addition, systematic differences exist between these two most precise data sets because of the target polarization, dilution factor, and the different impact from required model input for R and A_2 at different kinematics (see also Sec. V C below). The corresponding systematic uncertainties are indicated for EG1b by the shaded band at the bottom of the plot.

We also show various predictions based on expectations about the asymptotic value for A_1^d in the limit $x \to 1$ (see Sec. II C). The prediction from a SU(6)-symmetric quark model is a constant value of 1/3 for A_1^d and is indicated by the short horizontal line at the right-hand edge of the plot. A more advanced quark model including hyperfine perturbation through one-gluon exchange [32] yields a range of possible behaviors at high x, as indicated by the shaded

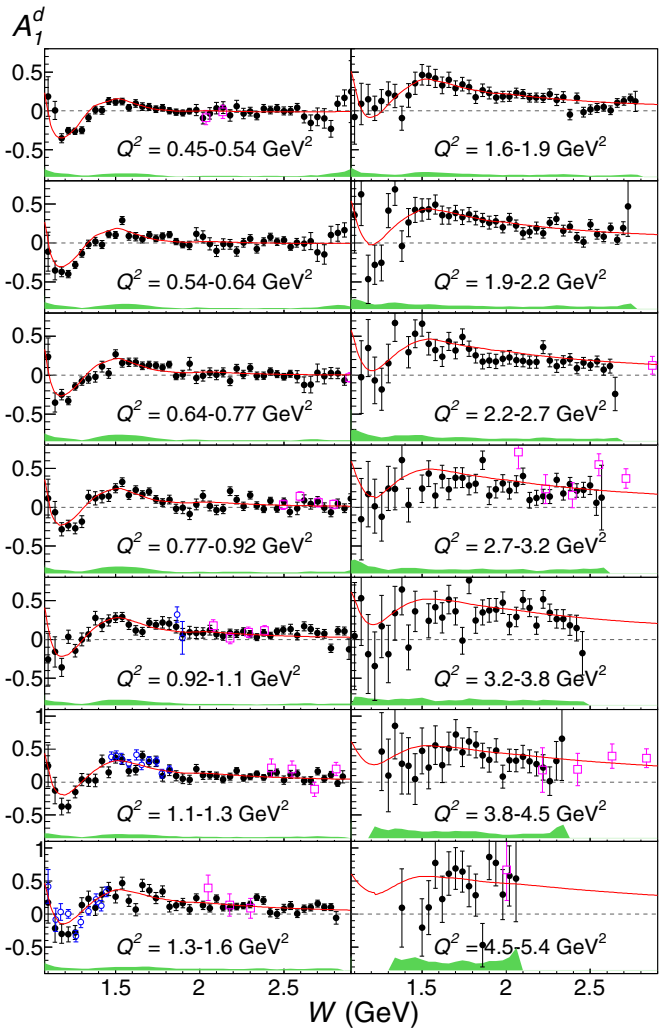

FIG. 11. (Color online) Continuation of Fig. 10 for the remaining Q^2 bins. In addition to our data and the SLAC data (see above), we also show the data from the Jefferson Lab RSS experiment [14,84] (blue open circles).

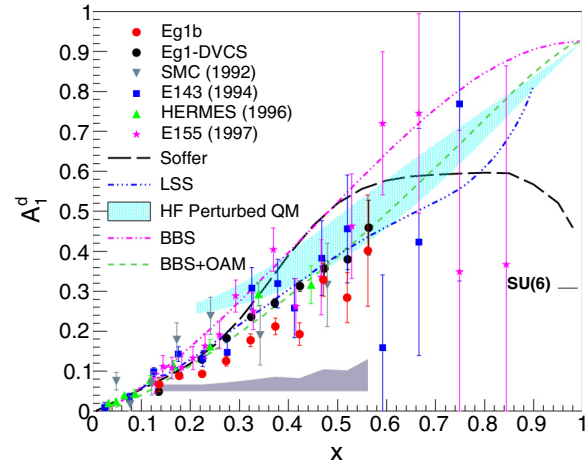

FIG. 12. (Color online) A_1^d versus x in the DIS region ($Q^2 > 1$ GeV^2 and $W > 2$ GeV) from EG1b and several other experiments: EG1-dvcs at Jefferson Lab [21], SMC at CERN [85], E143 and E155 at SLAC [15,17,83], and HERMES at DESY [18]. Statistical uncertainties are indicated by error bars, and EG1b systematic uncertainties are shown by the shaded band at the bottom. Various theoretical predictions and parametrizations are shown as lines and shaded band and are discussed in the text.

(light blue) band. Two different curves (labeled BBS) are based on pQCD models, one under the assumption of pure quark-hadron helicity conservation [33] and a second one including the effect of a possible nonzero orbital angular momentum (BBS + OAM [35]). Finally, we show two recent NLO parametrizations of the world data (by Soffer *et al.* [86] and by Leader, Stamenov, and Sidorov (LSS) [87]).

We note that, on average, the world data including our own indicate a rise of A_1^d beyond the SU(6) limit at very large x, but much slower than expected from pQCD without the inclusion of orbital angular momenta. Taking a possible Q^2 dependence and systematic uncertainties into account, our data agree best with the BBS model including orbital angular momenta [35] and are also compatible with the lower edge of the range of predictions from the hyperfine-perturbed quark model [32]. Overall, no firm conclusion can be drawn yet about the transition of the down quark polarization from negative values below $x \approx 0.5$ to the limit of $+1$ expected from pQCD. A similar conclusion comes from measurements on ^{3}He [12,88].

C. The spin structure function g_1

In addition to extracting A_1, we can also use the measured asymmetry $A_{||}$ to extract the spin structure function g_1^d according to Eq. (11). As a first step, we extract the ratio g_1^d/F_1^d, which is less sensitive to various model inputs. Figure 13 shows the resulting data, plotted for several x bins (all with a bin width of $\Delta x = 0.05$) versus the photon virtuality Q^2. Again, we also show world data for the same quantity. Our data agree reasonably well with those from E143 [15,83] within statistical uncertainties, but are somewhat lower than the very precise data from the recently published follow-up experiment EG1-dvcs [21]. The difference between these two experiments is consistent with the known uncertainty on their overall normalization, which is up to 14% for EG1b and around 8.5% for EG1-dvcs. These normalization uncertainties are completely uncorrelated between the two experiments, because they are dominated by the *statistical* uncertainties on the measured values of the product of target and beam polarization (see Sec. IV D 2).

The Q^2 dependence of g_1^d/F_1^d at lower Q^2 reflects the effect of nucleon resonances at $W < 2$ GeV, while beyond this limit (indicated by arrows on the x axis) this dependence is mild but still rising, indicating a smooth but not necessarily fast transition to the scaling region. We indicate the results for g_1/F_1 at $Q^2 = 5$ GeV^2 from a recent NLO fit of the world data [87] for comparison.

We then use models for the unpolarized structure function F_1 (see next section) to convert these ratios to g_1. The results for the product xg_1^d versus Bjorken x for each of our Q^2

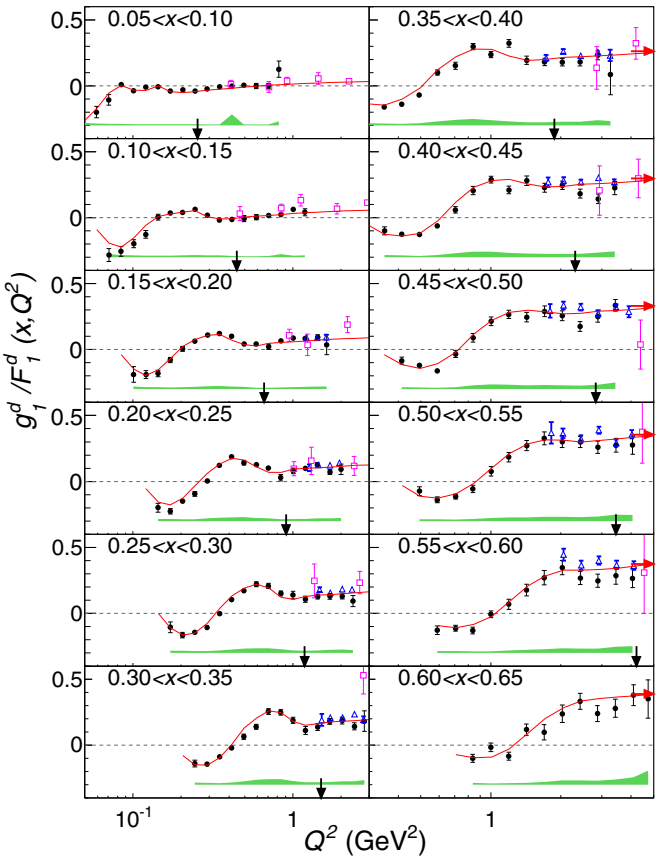

FIG. 13. (Color online) The ratio g_1/F_1 for the deuteron versus Q^2 and for various bins in the Bjorken variable x, together with our model shown as the red line on each plot. All data are corrected by our model to center them on the middle of each x bin. The shaded area at the bottom of each plot represents the systematic uncertainty. Published world data are shown as open magenta squares (E143 [15,83]) and open blue triangles (EG1-dvcs [21]). Arrows on the x axis indicate the limit $W = 2$ GeV. The horizontal arrows on the right-hand side of the right panel indicate the results for g_1/F_1 of a recent NLO analysis of world data [87] for our bin centers and $Q^2 = 5$ GeV^2.

bins are presented in Fig. 14, together with world data. The red curve on each plot comes from our model. At low Q^2, g_1 is strongly affected by resonance structures, in particular the $\Delta(1232)$ again being the most prominent one, making g_1 negative in this region. When we go to higher Q^2, the effect of the resonances diminishes and g_1 approaches the smooth DIS curve also shown in Fig. 14 as a blue dashed line. This can be interpreted as a sign that quark-hadron duality begins to work at these larger $Q^2 > 1.0$ GeV^2. However, in the $\Delta(1232)$ region, the data fall noticeably below the blue line even at Q^2 as high as $\approx$1GeV^2.

In the DIS region ($W > 2$ GeV and $Q^2 > 1$ GeV^2), $g_1^d(x)$ can be used to extract information on the quark helicity contributions to the nucleon spin (see Sec. II D). Comparing our data to the higher Q^2 data from COMPASS [20], one can extract information on the gluon polarization through DGLAP evolution. Including our data for somewhat lower Q^2, higher twist modifications of the polarized PDFs can be constrained. Our data are available for such PDF fits, similar to recent fits by the JAM Collaboration [80] and by Leader *et al.* [87], as well as for future tests of duality.

D. Models

To extract the physics quantities discussed above from our data on $A_{||}$, we require models both for the unpolarized structure functions F_1 and F_2 (or, equivalently, F_1 and R), as well as for the asymmetry A_2. These models (plus a model for the asymmetry A_1) are also needed to evaluate radiative corrections (Sec. IV D 5) and to extrapolate our data to small x for the purpose of evaluating moments of g_1 (see next section). For the deuteron case in particular, we need models for both the proton and the neutron, as well as a prescription for Fermi smearing.

We will describe our fit in detail in Ref. [22]. Our approach to Fermi smearing is explained in Sec. II G. Here we just summarize our sources of data for the fits to A_2 and A_1 for the proton and the neutron. For the unpolarized structure functions $F_1^{p,n}$ and $R^{p,n}$, we used a recent parametrization of the world data by Bosted and Christy [67,89]. This parametrization fits both DIS and resonance-region data with an average precision of 2%–5%, including Jefferson Lab Hall C data on the proton and the deuteron with very similar kinematics to ours. Systematic uncertainties due to these models were calculated by varying either F_1 or R by the average uncertainty of the fit and recalculating all quantities of interest.

For the asymmetries in the region $W > 2$ GeV, we developed our own phenomenological fit to the world data, including all DIS results from SLAC, HERA, CERN, and Jefferson Lab (see Ref. [1] for a complete list). In the resonance region, we added data from EG1a [23,71] in Hall B, RSS [14] in Hall C, and MIT-Bates [90]. We also used the data reported here and in Ref. [22] and iterated the fit after reextracting our data using the updated models. The proton asymmetries were fit first, followed by a fit to the neutron A_1 and A_2. For this second part, we used the rich data set collected on ^{3}He at Jefferson Lab (Hall A) [11,12,88,91,92], SLAC [93–96], and HERMES [18,97], as well as the world data on the deuteron, including our own. The goodness of the fit (χ^2) was calculated by comparing the fit functions for neutron asymmetries directly with neutron results extracted from ^{3}He data, as well as comparing the convolution of our proton and neutron models with corresponding deuteron data. To anchor our fit of A_1 at the photon point, we used data from ELSA and MAMI (see, e.g., the summary by Helbing [98]). As a result, we achieved a consistent fit of proton, deuteron, and neutron data over a wide kinematic range, far exceeding our own kinematic coverage. The overall χ^2 for the fit was 2451 for 3225 degrees of freedom.

Our fit results are shown as curves on most of the plots in this section, and they are generally in very good agreement with the existing data. We developed alternative model fits representing the uncertainty of our fit results in all cases and estimated the systematic uncertainties on all extracted quantities due to model uncertainties by replacing the standard fits, one by one, with these alternatives.

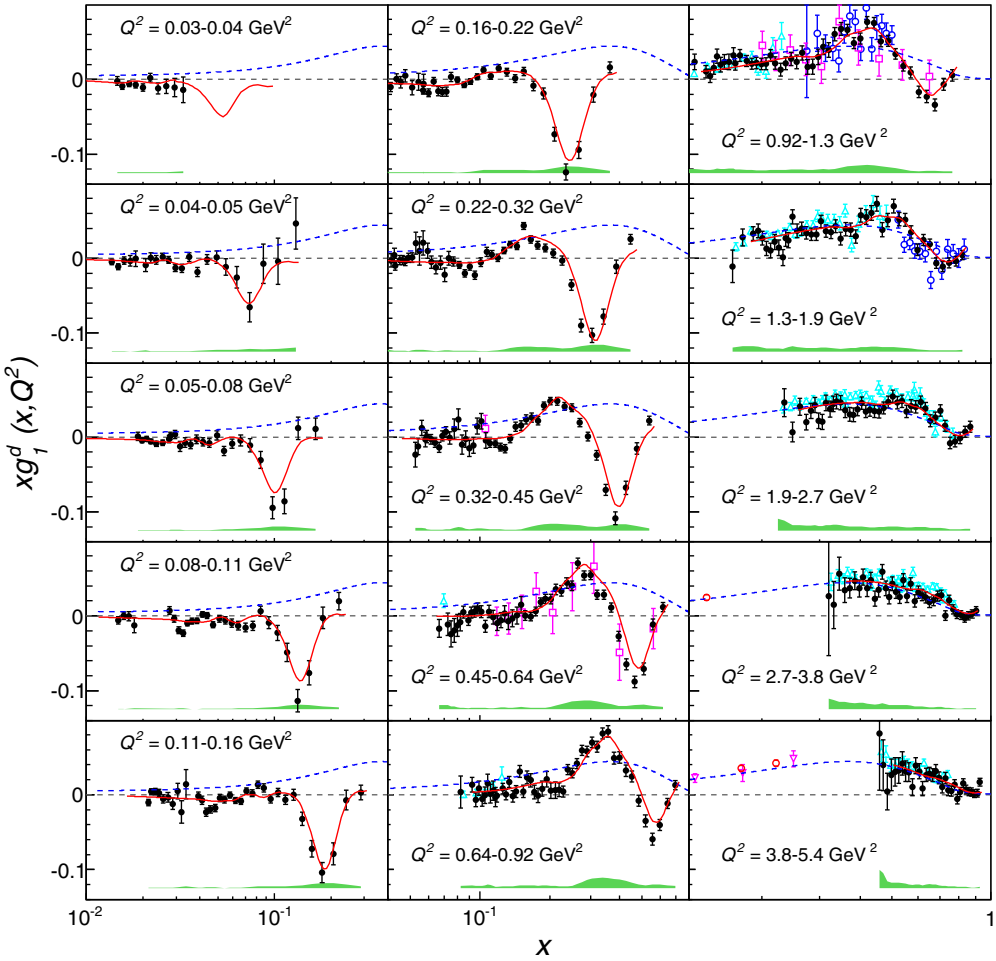

FIG. 14. (Color online) The product xg_1 versus x for all Q^2 bins, together with our model (red lines). The shaded area at the bottom of each plot represents the systematic uncertainty. The corresponding DIS parametrization for $Q^2 = 10$ GeV^2 is also shown (blue dashed lines). World data are shown for HERMES [18] (red circles), SLAC E143 [15,83] (open magenta squares), SLAC E155 [17] (magenta inverted triangles), RSS [14,84] (blue circles), and EG1-dvcs [21] (cyan triangles).

E. Moments of g_1

From our data, we determined several moments of spin structure functions. We evaluated those moments for each of our standard Q^2 bins in two parts. For W regions where we have good data (with reasonably small statistical uncertainties), we summed directly over these data (binned in 10-MeV bins in W), multiplied by the corresponding bin width in x and the required power of x. We avoided the region below $W = 1.15$ GeV, where radiative effects and the quasielastic contribution overwhelm the data. The upper end of the integration range can go up to $W = 3$ GeV, depending on the Q^2 bin. The resulting values of the integral over the kinematic region covered by our data are shown as the open (blue) circles in Fig. 15, and the properly propagated systematic uncertainty in the measured region is shown as the light beige band. Note that all moments are calculated per nucleon (i.e., divided by 2 for the two nucleons in deuterium), following common practice. However, we do *not* correct for the deuteron D state or any other nuclear effects.

We integrate our model for g_1^d (without any quasielastic contributions) over the region $1.08\ \text{GeV} \leqslant W \leqslant 1.15$ GeV to estimate this small part of the full moment.[2] Occasionally, there are gaps in our W coverage from different beam energies, especially at low Q^2 (see, e.g., Fig. 10). These gaps are also filled by integrating the model instead. Finally, we integrate the model from the lower x limit of our highest W bin (for each Q^2) down to $x = 0.001$. This contribution becomes most important at high Q^2 and for the lowest (first) moment. We limit ourselves to this minimum x value because there are no reliable data at lower x, and our model becomes unconstrained and rather uncertain below $x = 0.001$. While it is likely that there is no significant contribution below this limit,[3] we prefer to quote our results as moments from $x = 0.001$ to $x_{\max}$, where

$$x_{\max} = \frac{Q^2}{W_{\min}^2 - M^2 + Q^2} \tag{28}$$

[2]We exclude the (quasi-)elastic region $W < 1.08$ GeV, following common convention, because the quasielastic peak would overwhelm the integrals at small Q^2.

[3]The contribution from $x < 0.001$ is most certainly negligible for the higher moments.

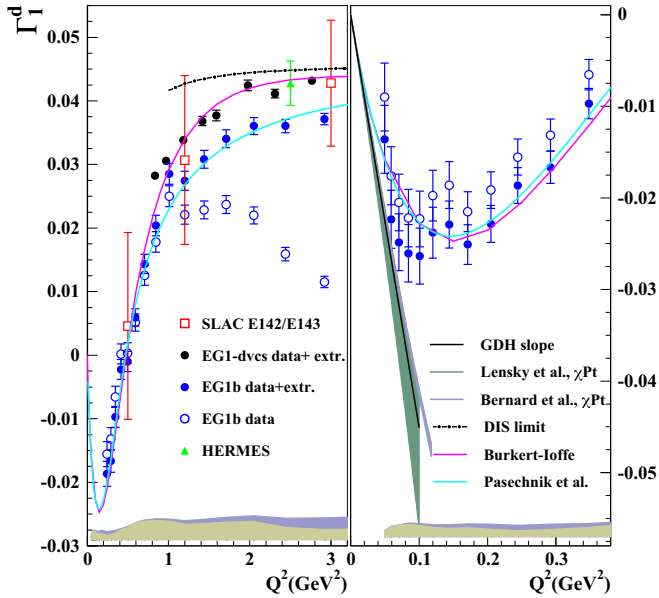

FIG. 15. (Color online) Γ_1 for the deuteron versus Q^2 from our data only (open blue circles) and from data plus model (solid blue circles), including the extrapolation to the unmeasured kinematics. The left-hand side shows the full Q^2 range (leaving out our data for $Q^2 < 0.3$ GeV^2, to avoid clutter) and the right-hand side focuses on the small-Q^2 region. The systematic uncertainty is shown at the bottom of the plot, for data only (light beige shaded area in the foreground) and for combined data and model (blue shade in the background). Corresponding results from SLAC E143 [15,83], HERMES [18], and EG1-dvcs [21] are shown, as well as several predictions (explained in the text).

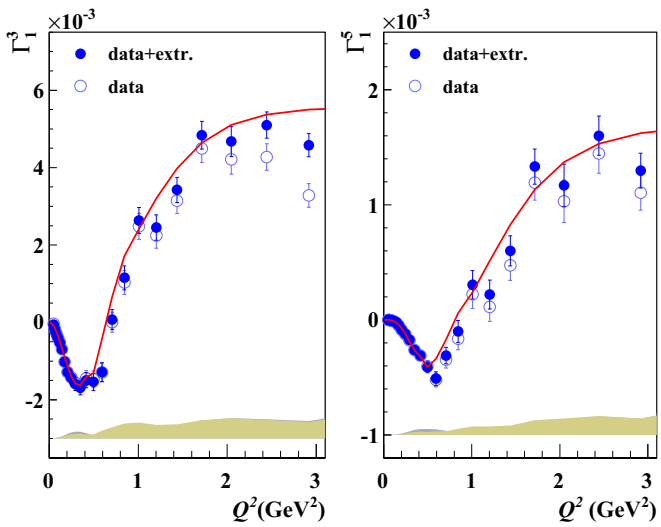

FIG. 16. (Color online) Higher moments of g_1^d extracted from the EG1b data versus Q^2. The third moment for the deuteron, Γ_1^3, is shown on the left, and the fifth moment, Γ_1^5, on the right. The open squares were calculated with no model contribution, while the solid squares include model input for the kinematic regions with no available data. The total systematic uncertainty is shown by the blue (experimental only) and black (experimental plus extrapolation) shaded areas.

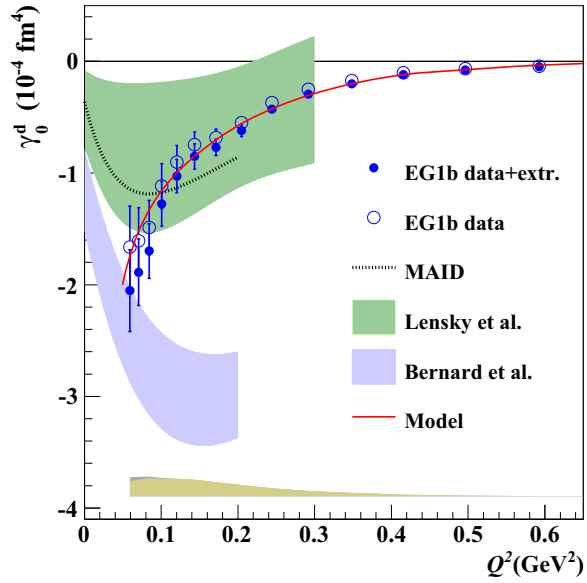

FIG. 17. (Color online) Forward spin polarizability (γ_0) for the deuteron versus Q^2. The open squares represent the result using only data and the solid black circles are data plus model results. The shaded area close to the x axis is the total systematic uncertainty (blue for experimental only and black with extrapolation uncertainty included). Our model is shown as a red solid line. Our results are compared to three χPT calculations (see text) and the MAID parametrization [102] for single-pion production.

and $W_{\rm min} = 1.08$ GeV. The values of the full integral for the first moment are shown in Fig. 15 as the solid (blue) data points and the full systematic uncertainty due to the additional model uncertainty in the unmeasured region is indicated by the wider blue band behind the beige one. We also show published world data on the first moment in the same Q^2 range. Our data are again in reasonable agreement with the world data (within statistical uncertainties) except for being slightly below the data from EG1-dvcs [21], as mentioned before; again, the difference is consistent with the systematic uncertainty on both experiments. At $Q^2 < 0.8$ GeV^2, ours are the only high-precision data available so far, extending down to $Q^2 = 0.05$ GeV^2, where they can be used to test effective theories like χPT.

We compare our results with several theoretical predictions and parametrizations in Fig. 15. The black dashed-dotted curve indicates the extrapolation from the DIS limit using pQCD corrections up to third order in α_s, assuming the asymptotic value for the moment from recent publications by COMPASS [19] and HERMES [18]. We also show two parametrizations that connect the DIS limit with the real photon point. One parametrization, by Burkert and Ioffe [99] (upper magenta curve), combines an estimate of the integral in the resonance region with a smooth function connecting the photon point, constrained by the GDH sum rule [44,45], with the asymptotic limit. The second, by Pasechnik *et al.* [100] (light blue line), includes both higher-twist terms at large Q^2 and a chiral-like expansion at the photon point within the framework of an analytic perturbation theory (APT) which has been fit to available data, including previous (partial) results

from EG1b [26]. Both parametrizations do a remarkably good job describing the world data on the first moment over the full range of Q^2.

We also show several predictions for the low-Q^2 behavior of Γ_1 on the right-hand side of Fig. 15, including the slope at $Q^2 = 0$ from the GDH sum rule [44,45] (solid black line) and its extensions from two recent χPT calculations. The first one, by Bernard *et al.* [38] (narrow dark gray band on right-hand side), is an expansion up to third order with explicit inclusion of $\Delta(1232)3/2^+$ isobar degrees of freedom. The second, by Lensky *et al.* [101] (wider dark green band), uses Baryon χPT including pion, nucleon, and $\Delta(1232)$ degrees of freedom to calculate all moments in NLO. Both predictions are close to the GDH limit and show little sign of the observed deviation of the data towards less negative values as Q^2 increases; however, they agree with our lowest three points $Q^2 < 0.08\,\mathrm{GeV}^2$ within their statistical and systematic uncertainties.

The higher moments Γ_1^3 and Γ_1^5 are also calculated in the same way with appropriate powers $n = 3,5$ (see Sec. II A). Figure 16 shows the results for the third moment Γ_1^3 and the fifth moment Γ_1^5 of g_1 from the EG1b data. These moments are useful for the extraction of higher-twist matrix elements; e.g., the third moment is directly related to the matrix element a_2 within the operator product expansion.

To calculate the extended spin polarizability γ_0, we integrate the product of A_1F_1 instead of g_1, weighted with x^2. The result is multiplied by $16M^2(\hbar c)^4\alpha/Q^6$ to convert to (10^{-4} fm^4), in agreement with the definition for real photons. Figure 17 shows our result for the forward spin polarizability γ_0 for the deuteron. We compare them again to the χPT calculations by Lensky *et al.* [101] (upper yellow band) and by Bernard *et al.* [38] (lower light blue band), as well as an evaluation of single-pion production data by the MAID Collaboration [102]. The χPT calculations do not quite reproduce the trend of the data at low Q^2.

F. Neutron spin structure functions

Although many data sets exist for spin structure functions of the (bound) neutron in the deep inelastic (DIS) region, no unintegrated results have been published in the region

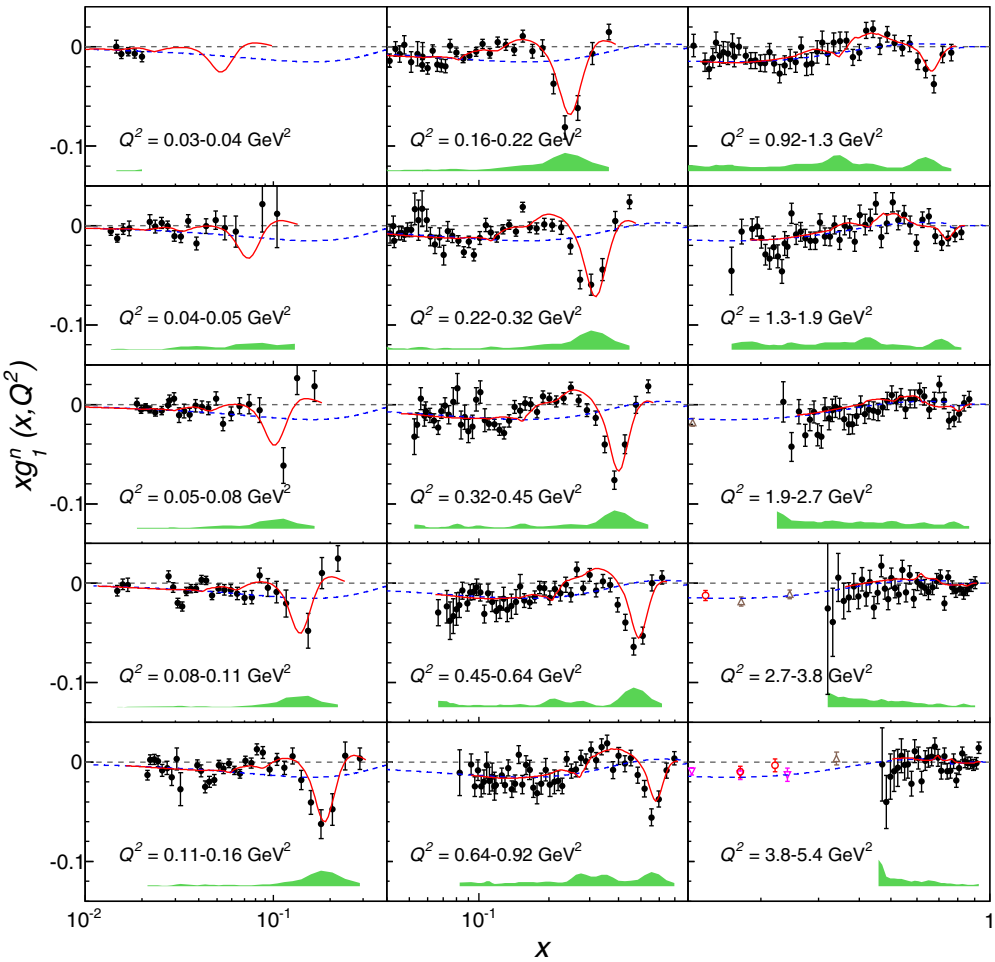

FIG. 18. (Color online) Our results for the spin structure function xg_1 of the bound neutron, extracted in the impulse approximation framework of Ref. [27] versus the Bjorken variable x for all (combined) Q^2 bins (solid circles). Our model is shown as red lines on each plot, and the asymptotic form of $g_1(x)$ in the DIS region is shown as dashed blue lines. The shaded area at the bottom of each plot represents the systematic uncertainty. Additional data from other experiments are shown as well: E154 [95] (magenta inverted triangles), HERMES [18,97] (red circles), and E142 [94] (brown triangles).

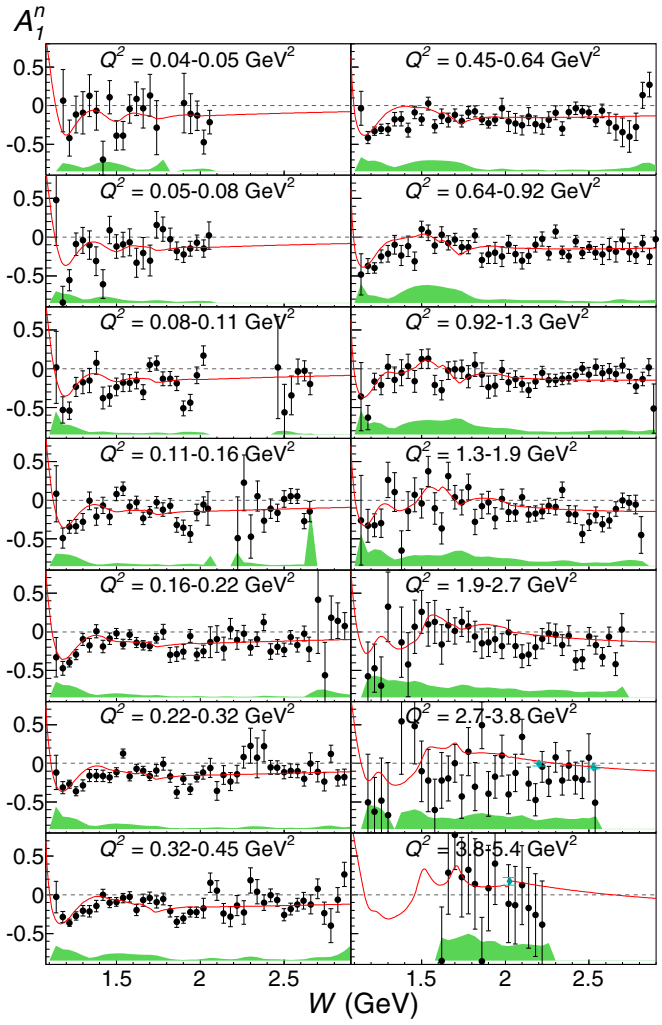

FIG. 19. (Color online) A_1 for the bound neutron, extracted from our results for g_1^n (see Fig. 18), versus W for our combined Q^2 bins. Systematic uncertainties are shown as the shaded area at the bottom of each plot. Our parametrized model is also shown as a red line on each plot. Only the data points with $\sigma_{\rm stat} < 0.6$ and $\sigma_{\rm sys} < 0.2$ are plotted. The cyan diamonds indicate data from measurements on ^{3}He [12,88].

$W < 2$ GeV of the nucleon resonances. This is attributable to the difficulty of reliably extracting neutron information from measurements that have to use nuclear targets, as explained in Sec. II G. As discussed in that section, we have attempted, for the first time, to combine our deuteron data with our proton fit (Sec. V D) and an impulse approximation folding prescription to access information on the neutron in a model-dependent way; see Figs. 18 and 19.

Our method relies on the folding prescription by Kahn *et al.* [27], which describes deuteron structure functions in terms of those of the proton and the neutron. We used this prescription in our fit for the asymmetries A_1^n and A_2^n for the neutron as described in Sec. V D. In particular, for any set of fit parameters, we calculate both g_1^n, g_2^n and g_1^p, g_2^p, combine them (following Ref. [27]), and compare directly to the measured g_1^d. The parameters are optimized until the best possible agreement (smallest χ^2) is achieved.

Our extraction of the g_1^n data points shown in Fig. 18 follows a slightly different procedure than that described in Ref. [27], but is similar to their "additive" method: We assume that any difference between the measured and the calculated g_1^d is solely attributable to a corresponding discrepancy in g_1^n at that specific kinematic point. Given that to first approximation

$$g_1^d \approx (1 - 1.5P_D)\left(g_1^n + g_1^p\right), \tag{29}$$

we then calculate

$$g_1^n(\text{meas}) = g_1^n(\text{model}) + \frac{g_1^d(\text{meas}) - g_1^d(\text{model})}{1 - 1.5P_D}, \tag{30}$$

with $P_D \approx 0.05$. This method has the advantage that it is stable (as opposed to trying to invert the folding) and that it leads to a straightforward propagation of statistical uncertainties:

$$\sigma\left(g_1^n\right)(\text{meas}) = \frac{\sigma\left(g_1^d\right)(\text{meas})}{1 - 1.5P_D}. \tag{31}$$

The systematic uncertainties are evaluated in the same fashion as in all previous cases (see Sec. IV D 6), by varying one model input or experimental parameter in sequence and propagating the variation to the final result for g_1^n(meas), then adding all of these variations in quadrature. The final results are shown in Fig. 18, together with world data at higher W and both our model parametrization (red line) and the DIS limit at $Q^2 = 10$ GeV^2 (blue dashed line). We combined our standard Q^2 bins pairwise for clarity of presentation.

As a next step, we can then convert the results for g_1^n into the virtual photon asymmetry A_1^n, by using our models for F_1^n and A_2^n. The results are shown in Fig. 19. Overall, the agreement of the extracted results with our model is quite good, except at the highest Q^2, where our data seem to lie systematically lower (a trend that can already be observed in the corresponding deuteron data; see Fig. 11). We direct the attention of the reader to the additional data points plotted in the last two Q^2 bins (cyan diamonds); these are the results from the Hall A experiment on ^{3}He [12,88] at the highest attainable x in the DIS region. These data are consistent with our own, but with significantly smaller statistical uncertainties. However, no such data have been published for any of the lower Q^2 bins.

As a final step, we once again form various moments of the neutron spin structure functions (see Figs. 20 and 21). While the advantage of using deuterium as a proxy for the neutron (namely, its much smaller average nucleon momenta and therefore less severe kinematic smearing) is less clear in this case (because the moments integrate over all kinematics anyway), it is still instructive to compare our results to those using a ^{3}He target as a source of polarized neutrons [11]. Again, we find good agreement between these two experiments using different effective neutron targets and with very different systematic uncertainties. We note that the neutron data are also well described by the two parametrizations [99,100], while they approach the GDH limit above (but marginally compatible with) the chiral perturbation calculations [38,101].

Figure 21 shows the forward spin polarizability for the bound neutron from our data, again compared to data from the ^{3}He experiment in Hall A [11]. The agreement at the lowest

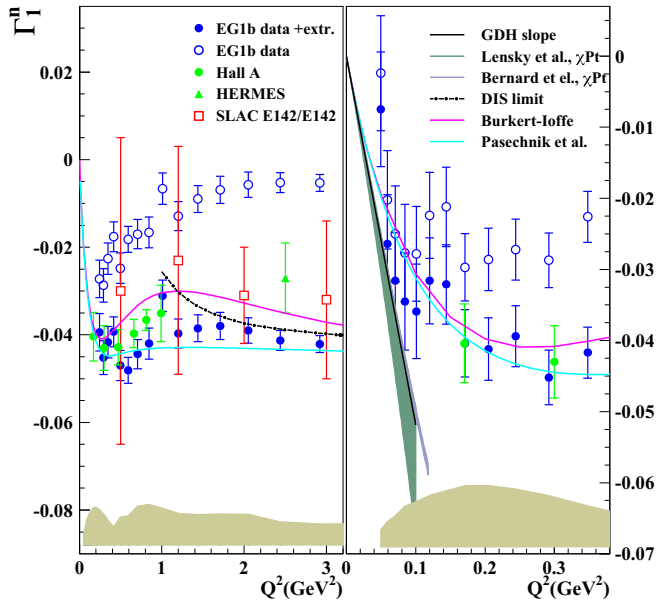

FIG. 20. (Color online) Γ_1 for the neutron versus Q^2 from data only (open blue circles) and data plus model (solid blue circles), including the extrapolation to the unmeasured kinematics. Also shown are phenomenological calculations from Pasechnik *et al.* [100] (lower light blue line) and Burkert and Ioffe [99] (upper magenta line), together with the χPT results from Lensky *et al.* [101] (wider dark green band) and Bernard *et al.* [38] (thin gray band). The GDH slope (black solid line) and pQCD prediction (black dotted line) are also shown. The right-hand side plot is a magnification of the low Q^2 region (which is omitted from the left-hand side). Systematic uncertainties of our data are shown as shaded areas at the bottom of the plot. Results from other experiments are also shown, with statistical and systematic uncertainties (added in quadrature) reflected in their total error bars.

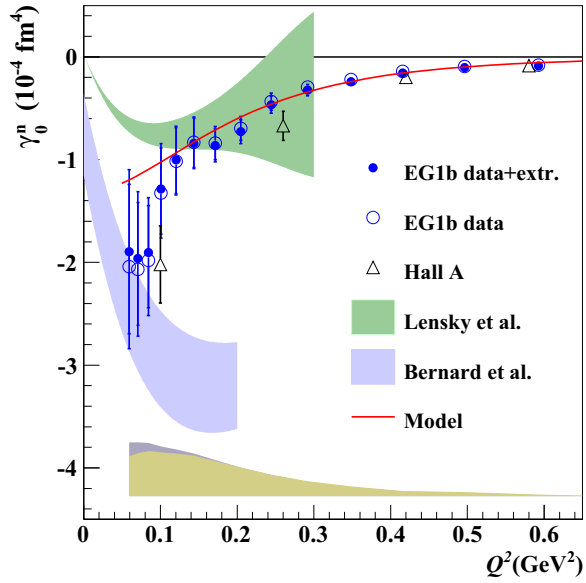

FIG. 21. (Color online) Forward spin polarizability γ_0 for the neutron versus Q^2. The open squares represent the result using only data and the solid black circles are data plus model results. The shaded area close to the x axis is the total systematic uncertainty (blue for experimental data only and black including the extrapolation). Our model is also shown as a red solid line. Our results are compared to three χPT calculations (see text) and to the ^{3}He data from Hall A [11].

Q^2 is excellent, and our data extend to slightly lower Q^2. Once again, they show a general agreement with the order of magnitude predicted by χPT, while exhibiting a distinctly different shape with Q^2.

VI. CONCLUSION

In summary, we present the final analysis of the most extensive data set on the spin structure functions A_1 and g_1 of the deuteron in the valence and resonance region. The data cover two orders of magnitude in squared momentum transfer, $0.05 \leqslant Q^2 \leqslant 5$ GeV^2, connecting the region of hadronic degrees of freedom and effective theories like χPT near the photon point with the regime where pQCD is applicable. Our data give more detailed insight in the inclusive response of the deuteron in the resonance region and how it connects with the DIS limit. They can constrain NLO fits (including higher-twist corrections) of spin structure functions extracting polarized PDFs, and they shed new light on the valence quark structure of the nucleon at large x. They can be used to study quark-hadron duality and to extract matrix elements in the framework of the operator product expansion. To facilitate such analyses, we are providing the raw data (with minimum theoretical bias) through the CLAS experimental database [81] as well as Supplemental Material for this paper [82].

We use our data on the deuteron, together with a detailed fit of the corresponding proton data, to extract bound neutron spin structure functions, using a convolution model and ignoring FSI and other binding effects. These results give information, for the first time, on inclusive neutron spin structure in the resonance region $W < 2$ GeV. They can also be used to cross-check the results from ^{3}He targets at high x. We find general agreement between the data from these rather different approaches, within the relatively larger statistical uncertainties of our data set. However, our data cover a larger range in Q^2 and W.

Our data allow precise determinations of moments of g_1^d (and g_1^n) as a function of Q^2, which can be used to test the approach to the GDH sum rule limit, χPT, and phenomenological models, and to extract matrix elements in the framework of the operator product expansion. We find that χPT describes our results for Γ_1 only up to very moderate $Q^2 \approx 0.08$ GeV^2 (within our statistical and systematic uncertainties), while there is only rough agreement in magnitude between χPT and our data for the forward spin polarizability γ_0. Finally, we would like to refer the reader to a recent analysis of the world data [103], including the data presented here, to study the first moment of the difference $g_1^p - g_1^n$ and its Q^2 dependence to extract operator product expansion (OPE) matrix elements.

Further data will come from the analysis of the EG4 experiment with CLAS, which will extend the kinematic coverage of the present data set to even lower Q^2 for a more rigorous test of χPT. Additional information on the structure

functions g_2 and A_2 is forthcoming once experiment "SANE" in Hall C and experiment "g2p" in Hall A have been analyzed. Finally, a complete mapping of spin structure functions in the valence quark region, out to the highest possible x, is one of the cornerstones of the program with the energy-upgraded 12-GeV accelerator at Jefferson Lab.

ACKNOWLEDGMENTS

This material is based upon work supported by the US Department of Energy, Office of Science, Office of Nuclear Physics under Contracts No. DE-AC05-06OR23177 and No. DE-FG02-96ER40960 and other contracts. Jefferson Science Associates (JSA) operates the Thomas Jefferson National Accelerator Facility for the United States Department of Energy. We would like to acknowledge the outstanding efforts of the staff of the Accelerator and the Physics Divisions at Jefferson Lab that made this experiment possible. This work was supported in part by the US National Science Foundation, the Italian Instituto Nazionale di Fisica Nucleare, the French Centre National de la Recherche Scientifique, the French Commissariat à l'Energie Atomique, the Emmy Noether grant from the Deutsche Forschungs Gemeinschaft, the Scottish Universities Physics Alliance (SUPA), the United Kingdom's Science and Technology Facilities Council, the Chilean Comisión Nacional de Investigación Científica y Tecnológica (CONICYT), and the National Research Foundation of Korea.

[1] S. Kuhn, J.-P. Chen, and E. Leader, Prog. Part. Nucl. Phys. **63**, 1 (2009).
[2] Y. L. Dokshitzer, Sov. Phys. JETP **46**, 641 (1977).
[3] V. N. Gribov and L. N. Lipatov, Yad. Fiz. **15**, 781 (1972).
[4] G. Altarelli and G. Parisi, Nucl. Phys. B **126**, 298 (1977).
[5] E. V. Shuryak and A. I. Vainshtein, Nucl. Phys. B **201**, 141 (1982).
[6] E. V. Shuryak and A. I. Vainshtein, Nucl. Phys. B **199**, 451 (1982).
[7] B. Ehrnsperger, A. Schafer, and L. Mankiewicz, Phys. Lett. B **323**, 439 (1994).
[8] E. D. Bloom and F. J. Gilman, Phys. Rev. Lett. **25**, 1140 (1970).
[9] W. Melnitchouk, R. Ent, and C. Keppel, Phys. Rep. **406**, 127 (2005).
[10] W. Cosyn, W. Melnitchouk, and M. Sargsian, Phys. Rev. C **89**, 014612 (2014).
[11] M. Amarian *et al.* (Jefferson Lab E94-010 Collaboration), Phys. Rev. Lett. **92**, 022301 (2004).
[12] X. Zheng *et al.* (Jefferson Lab Hall A Collaboration), Phys. Rev. C **70**, 065207 (2004).
[13] P. Solvignon *et al.* (Jefferson Lab E01-012 Collaboration), Phys. Rev. Lett. **101**, 182502 (2008).
[14] F. R. Wesselmann *et al.* (RSS Collaboration), Phys. Rev. Lett. **98**, 132003 (2007).
[15] K. Abe *et al.* (E143 collaboration), Phys. Rev. D **58**, 112003 (1998).
[16] B. Adeva *et al.* (Spin Muon Collaboration), Phys. Rev. D **58**, 112002 (1998).
[17] P. Anthony *et al.* (E155 Collaboration), Phys. Lett. B **463**, 339 (1999).
[18] A. Airapetian *et al.* (HERMES Collaboration), Phys. Rev. D **75**, 012007 (2007).
[19] V. Alexakhin *et al.* (COMPASS Collaboration), Phys. Lett. B **647**, 8 (2007).
[20] E. Ageev *et al.* (COMPASS Collaboration), Phys. Lett. B **647**, 330 (2007).
[21] Y. Prok *et al.* (CLAS Collaboration), Phys. Rev. C **90**, 025212 (2014).
[22] R. Fersch *et al.* (CLAS Collaboration) (to be published).
[23] J. Yun *et al.* (CLAS Collaboration), Phys. Rev. C **67**, 055204 (2003).
[24] K. Dharmawardane *et al.* (CLAS Collaboration), Phys. Lett. B **641**, 11 (2006).
[25] P. Bosted, K. Dharmawardane *et al.*, Phys. Rev. C **75**, 035203 (2007).
[26] Y. Prok *et al.* (CLAS Collaboration), Phys. Lett. B **672**, 12 (2009).
[27] Y. Kahn, W. Melnitchouk, and S. A. Kulagin, Phys. Rev. C **79**, 035205 (2009).
[28] W. Meyer, K. Althoff, V. Burkert, U. Hartfiel, T. Hewel *et al.*, Nucl. Instrum. Methods Phys. Res., Sect. A **244**, 574 (1986).
[29] A. Airapetian *et al.* (HERMES Collaboration), Phys. Rev. Lett. **95**, 242001 (2005).
[30] O. Greenberg and M. Resnikoff, Phys. Rev. **163**, 1844 (1967).
[31] N. Isgur, G. Karl, and R. Koniuk, Phys. Rev. Lett. **41**, 1269 (1978).
[32] N. Isgur, Phys. Rev. D **59**, 034013 (1999).
[33] S. J. Brodsky, M. Burkardt, and I. Schmidt, Nucl. Phys. B **441**, 197 (1995).
[34] G. R. Farrar and D. R. Jackson, Phys. Rev. Lett. **35**, 1416 (1975).
[35] H. Avakian, S. J. Brodsky, A. Deur, and F. Yuan, Phys. Rev. Lett. **99**, 082001 (2007).
[36] S. Jeschonnek and J. W. Van Orden, Phys. Rev. C **80**, 054001 (2009).
[37] X.-D. Ji, C.-W. Kao, and J. Osborne, Phys. Lett. B **472**, 1 (2000).
[38] V. Bernard, E. Epelbaum, H. Krebs, and Ulf-G. Meißner, Phys. Rev. D **87**, 054032 (2013).
[39] J. Bjorken, Phys. Rev. **148**, 1467 (1966).
[40] J. Bjorken, Phys. Rev. D **1**, 1376 (1970).
[41] A. V. Sidorov and C. Weiss, Phys. Rev. D **73**, 074016 (2006).
[42] I. Balitsky, V. M. Braun, and A. Kolesnichenko, Phys. Lett. B **242**, 245 (1990).
[43] D. Dolgov, R. Brower, J. W. Negele, and A. Pochinsky, Nucl. Phys. Proc. Suppl. **73**, 300 (1999).
[44] S. Gerasimov, Sov. J. Nucl. Phys. **2**, 430 (1966).
[45] S. Drell and A. C. Hearn, Phys. Rev. Lett. **16**, 908 (1966).
[46] M. Gorchtein, D. Drechsel, M. M. Giannini, E. Santopinto, and L. Tiator, Phys. Rev. C **70**, 055202 (2004).
[47] C. Ciofi degli Atti, L. Kaptari, S. Scopetta, and A. Y. Umnikov, Phys. Lett. B **376**, 309 (1996).
[48] R. B. Wiringa, V. G. J. Stoks, and R. Schiavilla, Phys. Rev. C **51**, 38 (1995).

[49] S. P. Malace, Y. Kahn, W. Melnitchouk, and C. E. Keppel, Phys. Rev. Lett. **104**, 102001 (2010).
[50] L. P. Kaptari, A. Y. Umnikov, C. Ciofi degli Atti, S. Scopetta, and K. Y. Kazakov, Phys. Rev. C **51**, 52 (1995).
[51] L. L. Frankfurt and M. I. Strikman, Phys. Rep. **76**, 215 (1981).
[52] L. L. Frankfurt and M. I. Strikman, Phys. Rep. **160**, 235 (1988).
[53] I. Schmidt and J.-J. Yang, Eur. Phys. J. C **20**, 63 (2001).
[54] S. Tkachenko, N. Baillie, S. Kuhn *et al.*, Phys. Rev. C **89**, 045206 (2014).
[55] C. Leeman, D. Douglas, and G. Krafft, Annu. Rev. Nucl. Part. Sci. **51**, 413 (2001).
[56] C. Sinclair, P. Adderley, B. Dunham, J. Hansknecht, P. Hartmann *et al.*, Phys. Rev. Spec. Top.–Accel. Beams **10**, 023501 (2007).
[57] R. Kazimi, K. Beard, J. F. Benesch, A. Freyberger, J. Grames *et al.*, Proceedings of EPAC 2004, EPAC-2004-TUPLT164, JLAB-ACO-04-251 (2004).
[58] M. Stutzman, P. Adderley, J. Brittian, J. Clark, J. Grames *et al.*, Nucl. Instrum. Methods Phys. Res., Sect. A **574**, 213 (2007).
[59] W. de Boer, CERN 74-11, Laboratory I, Nuclear Physics Division (1974).
[60] M. Borghini, CERN 68-32, Nuclear Physics Division (1974).
[61] D. Crabb and W. Meyer, Ann. Rev. Nucl. Part. Sci. **47**, 67 (1997).
[62] B. Mecking *et al.*, Nucl. Instrum. Methods Phys. Res., Sect. A **503**, 513 (2003).
[63] M. Mestayer, D. Carman, B. Asavapibhop, F. Barbosa, P. Bonneau *et al.*, Nucl. Instrum. Methods Phys. Res., Sect. A **449**, 81 (2000).
[64] G. Adams, V. Burkert, R. Carl, T. Carstens, V. Frolov *et al.*, Nucl. Instrum. Methods Phys. Res., Sect. A **465**, 414 (2001).
[65] M. Amarian, G. Asrian, K. Beard, W. Brooks, V. Burkert *et al.*, Nucl. Instrum. Methods Phys. Res., Sect. A **460**, 239 (2001).
[66] E. Smith, T. Carstens, J. Distelbrink, M. Eckhause, H. Egiian *et al.*, Nucl. Instrum. Methods Phys. Res., Sect. A **432**, 265 (1999).
[67] M. E. Christy and P. E. Bosted, Phys. Rev. C **81**, 055213 (2010).
[68] P. Bosted *et al.* (CLAS Collaboration), Phys. Rev. C **78**, 015202 (2008).
[69] P. Norton, Rep. Prog. Phys. **66**, 1253 (2003).
[70] L. W. Mo and Y.-S. Tsai, Rev. Mod. Phys. **41**, 205 (1969).
[71] R. Fatemi *et al.* (CLAS Collaboration), Phys. Rev. Lett. **91**, 222002 (2003).
[72] C. Keith, M. Anghinolfi, M. Battaglieri, P. E. Bosted, D. Branford *et al.*, Nucl. Instrum. Methods Phys. Res., Sect. A **501**, 327 (2003).
[73] J. Arrington, Phys. Rev. C **69**, 022201 (2004).
[74] D. Crabb and D. Day, Nucl. Instrum. Methods Phys. Res., Sect. A **356**, 9 (1995).
[75] O. A. Rondon, Phys. Rev. C **60**, 035201 (1999).
[76] M. Mayer, Tech. Rep. CLAS-NOTE 2012-004, JLAB (2012).
[77] R. Dalitz, Proc. Phys. Soc. A **64**, 667 (1951).
[78] T. Gehrmann and M. Stratmann, Phys. Rev. D **56**, 5839 (1997).
[79] T. Kukhto and N. Shumeiko, Nucl. Phys. B **219**, 412 (1983).
[80] P. Jimenez-Delgado, A. Accardi, and W. Melnitchouk, Phys. Rev. D **89**, 034025 (2014).
[81] Jefferson Lab Experiment CLAS Database, http://clasweb.jlab.org/physicsdb
[82] See Supplemental Material at http://link.aps.org/supplemental/10.1103/PhysRevC.92.055201 for data tables for all figures.
[83] K. Abe *et al.* (E143 Collaboration), Phys. Rev. Lett. **78**, 815 (1997).
[84] O. A. Rondón, AIP Conf. Proc. **1155**, 82 (2009).
[85] B. Adeva *et al.* (Spin Muon Collaboration), Phys. Rev. D **58**, 112001 (1998).
[86] J. Soffer, C. Bourrely, and F. Buccella, Int. J. Mod. Phys. Conf. Ser. **37**, 1560052 (2015).
[87] E. Leader, A. V. Sidorov, and D. B. Stamenov, Phys. Rev. D **91**, 054017 (2015).
[88] X. Zheng *et al.* (Jefferson Lab Hall A Collaboration), Phys. Rev. Lett. **92**, 012004 (2004).
[89] P. E. Bosted and M. E. Christy, Phys. Rev. C **77**, 065206 (2008).
[90] O. Filoti, Ph.D. thesis, University of New Hampshire, 2007.
[91] K. Kramer, D. Armstrong, T. Averett, W. Bertozzi, S. Binet *et al.*, Phys. Rev. Lett. **95**, 142002 (2005).
[92] Z. Meziani, W. Melnitchouk, J.-P. Chen, S. Choi, T. Averett *et al.*, Phys. Lett. B **613**, 148 (2005).
[93] P. Anthony *et al.* (E142 Collaboration), Phys. Rev. Lett. **71**, 959 (1993).
[94] P. Anthony *et al.* (E142 Collaboration), Phys. Rev. D **54**, 6620 (1996).
[95] K. Abe *et al.* (E154 Collaboration), Phys. Rev. Lett. **79**, 26 (1997).
[96] K. Abe *et al.* (E154 Collaboration), Phys. Lett. B **404**, 377 (1997).
[97] K. Ackerstaff *et al.* (HERMES Collaboration), Phys. Lett. B **404**, 383 (1997).
[98] K. Helbing, Prog. Part. Nucl. Phys. **57**, 405 (2006).
[99] V. D. Burkert and B. L. Ioffe, J. Exp. Theor. Phys. **78**, 619 (1994).
[100] R. S. Pasechnik, J. Soffer, and O. V. Teryaev, Phys. Rev. D **82**, 076007 (2010).
[101] V. Lensky, J. M. Alarcón, and V. Pascalutsa, Phys. Rev. C **90**, 055202 (2014).
[102] S. Kamalov, D. Drechsel, O. Hanstein, L. Tiator, and S. Yang, Nucl. Phys. A **684**, 321 (2001).
[103] A. Deur, Y. Prok *et al.*, Phys. Rev. D **90**, 012009 (2014).